Delft University of Technology

L1 Adaptive Augmentation of an Incremental Nonlinear Dynamic Inversion Autopilot for Dual-Spin Guided Projectiles

Pineau, Sofiane ; Theodoulis, S.T.; Zasadzinski, Michel ; Boutayeb, Mohamed ; Roussel, Emmanuel

$\mathcal{L}_1$ Adaptive Augmentation of an Incremental Nonlinear Dynamic Inversion Autopilot for Dual-Spin Guided Projectiles

Sofiane Pineau*

University of Lorraine, CRAN-UMR-CNRS-7039, France. and French-German Research Institute of Saint-Louis, Department of Guidance, Navigation and Control, 68300, Saint-Louis, France

Spilios Theodoulis[†]

Delft University of Technology, Control & Simulation Section, 2629, HS Delft, The Netherlands

Michel Zasadzinski [‡] and Mohamed Boutayeb [§]

University of Lorraine, CRAN-UMR-CNRS-7039, 54400, Longwy, France

Emmanuel Roussel [¶]

French-German Research Institute of Saint-Louis, Department of Guidance, Navigation and Control, 68300, Saint-Louis, France

This article covers the design of an $\mathcal{L}_1$-adaptive Incremental Nonlinear Dynamic Inversion (INDI) autopilot applied to the control of the ballistic trajectory of a 155mm dual-spin projectile supplied with a roll-decoupled course-correction fuze. Associated with a Zero Effort Miss guidance law, the discrete-time INDI baseline successfully controls the lateral load factors of the projectile, resulting in a ballistic dispersion reduced to metric precision. However, aerodynamic data for dual-spin projectiles are often not very accurate because they rely on simplified CFD simulation and time-consuming wind tunnel tests aren't always possible. Therefore significant parametric uncertainties are present in the model. Even if INDI is a sensor-based control technique, this approach is still sensitive to model mismatch. For this reason, $\mathcal{L}_1$-adaptive control theory was used to compensate for the degraded inversion of the INDI autopilot under the presence of parametric uncertainties. Nonlinear simulation results show the interest of an $\mathcal{L}_1$-adaptive augmentation of an INDI autopilot where the performance of the autopilot is guaranteed under a large range of time-varying matched uncertainties.

I. Introduction

The general context of this article comes from the observation of a common lack of precision regarding standard 155mm spin-stabilized ammunition. As a matter of fact, this class of projectiles is known to suffer from ballistic dispersion toward the mission target and some solutions in the literature can be found to correct spin-stabilized projectiles deviation using impulse thrusters [1] or canards[2]. The considered corrective device is part of the latter approach, it consists of equipping existing shells with a roll-decoupled guidance fuze which includes embedded guidance and control laws, two pairs of canards and necessary sensors. This so-called dual-spin guided projectile is then expected to have a reduced ballistic dispersion and reach sub-metric precision.

The dynamics of dual-spin projectiles is nonlinear with many varying parameters because of its aerodynamics. Moreover, the lateral dynamics are strongly coupled due to the high spin rate of the main body of the projectile. All these elements make the control of the projectile difficult by the means of classical and linear control techniques like gain-scheduling [2, 3] because linear controllers designed for numerous operating points are needed to cover the flight envelope. Besides, gain-scheduling can guarantee performance and stability only locally around these flight points [4].

On the other hand, nonlinear control techniques are a relevant alternative to gain-scheduling because they avoid the local linearization procedure. Among them, Incremental Nonlinear Dynamic inversion is a sensor-based methodology which was used successfully in several aerospace applications in the latter years [5–7]. An interesting aspect of INDI is

---

*Phd student

[†]Assiociate professor

[‡]Professor in automatic control

[§]Professor in automatic control

[¶]Mecatronics and control Research scientist

its capacity to perform dynamic inversion with only a reduced part of the dynamical model which renders the control law more robust to model mismatch. For this reason, INDI was used in the article as a baseline autopilot for the control of the fuze roll motion and the projectile trajectory .

However, parameters related to control effectiveness of the system are involved in the INDI inversion and therefore uncertainties on these parameters affect INDI performance and stability. As a matter of fact, aerodynamic coefficients, especially those related to the canards aerodynamics are not precisely known. The inaccuracy of Computational Fluid Dynamics (CFD) simulations and the time-consumption of wind tunnel tests motivate the need for a control design approach which doesn't rely on a precise model and can tolerate a large range of uncertainties.

In order to guarantee the performance of the autopilot even under a large range of parametric uncertainties, $\mathcal{L}_1$ adaptive control theory was used to counteract the degraded dynamic inversion. More precisely, the roll and lateral channels INDI autopilot were augmented with a $\mathcal{L}_1$ adaptive scheme similarly to [8, 9]. In opposition to Model Reference Adaptive Control (MRAC), $\mathcal{L}_1$ theory offers a decoupling between adaptation and robustness by the mean of an underlying low pass filter. This decoupling is appealing when applied to the considered guided projectile because the embedded CPU has a limited frequency and the control law may be subjected to delays. By this filter, $\mathcal{L}_1$ theory guarantee minimal time-delay margin with fast adaptation[10].

The paper is organized as follows: Section II summarizes the nonlinear flight dynamics model of the dual-spin projectile, in Section III the design of the INDI baseline autopilot is detailed with analytical investigation of INDI inversion in discrete-time and with non-perfects actuators. Then, Section IV is dedicated to the $\mathcal{L}_1$ adaptive augmentation of the roll and lateral channels autopilot.

II. Flight Dynamics Modeling

The considered decoupled fuze guided projectile is represented by Fig. 1. It has two independent roll motions due to its dual-spin configuration. The main body is rotating at 300 Hz to maintain the projectile stability and the fuze roll is controlled by the canards and is stabilized during the controlled phase of the trajectory. Because of the extra roll motion of the fuze, the flight dynamics model described in Section II is called a 7DoF model.

A. Frames and Coordinate systems

The Earth inertial frame E is used as a reference frame. The projectile has a limited range (<30 kms) therefore a flat earth assumption is considered and a local geodesic coordinate system $]^L$ with (North, East, Down) directions is employed. The projectile has two frames related to its two separated parts: B_1 is linked to the main body and B_2 to the fuze. The dynamic equations are expressed in a non-rolling Body Fixed Frame (BFR) related coordinate system $]^{B_1'}$ [11], it undergoes the same movement as the main body of the projectile except for the roll motion which is fixed: $\phi_{BFR} = 0$ deg. The use of BFR avoids the simulator to integrate the high spin rate of the projectile which naturally demands a small integration step and could lead to numerical errors.
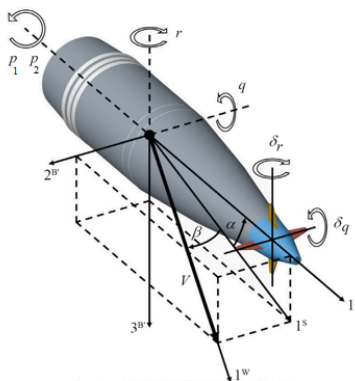

Fig. 1   Decoupled Fuze Guided Projectile

B. Translation and Attitude Dynamics

The Newton translation equation (1) describes the velocity of the projectile center of mass B with respect to the Earth inertial frame E expressed in the $]^{B'_1}$ coordinate system [12].

$$[f_B]^{B'_1} = m^B \left[\frac{dv_B^E}{dt}\right]^{B'_1} + m^B \left[\Omega^{B'_1 E}\right]^{B'_1} \left[v_B^E\right]^{B'_1} \tag{1a}$$

$$\begin{bmatrix} \dot{u} \\ \dot{v} \\ \dot{w} \end{bmatrix} = \left(\frac{1}{m^B}\right) \begin{bmatrix} X \\ Y \\ Z \end{bmatrix} - \begin{bmatrix} 0 & -r & q \\ r & 0 & r\tan\theta \\ -q & -r\tan\theta & 0 \end{bmatrix} \begin{bmatrix} u \\ v \\ w \end{bmatrix} \tag{1b}$$

In Eq (1a), $\left[v_B^E\right]^{B'_1} = [u \quad v \quad w]^\top$ is the velocity vector of the projectile c.m. B with respect to the Earth frame E, $\left[\Omega^{B'_1 E}\right]$ is the skew-symmetric form of the non-rolling frame rate vector $\left[\omega^{B'_1 E}\right]^{B'_1}$. m^B is the projectile total mass and $[f_B]^{B'_1} = [X \quad Y \quad Z]^\top$ is the external forces applied on the projectile detailed in Section II.D. The equation (1b) is obtained by isolating $\left[dv_B^E/dt\right]^{B'_1}$ and reformulate Eq (1a) in matrix form.

$$\left[m_{B_1}\right]^{B'_1} = \left[\tilde{I}_B^{B_{12}}\right]^{B'_1} \left[\frac{d\omega^{B_1 E}}{dt}\right]^{B'_1} + \left[\Omega^{B'_1 E}\right]^{B'_1} \left[\tilde{I}_B^{B_{12}}\right]^{B'_1} \left[\omega^{B_1 E}\right]^{B'_1} \tag{2a}$$

$$\left[m_{B_2}\{1,1\}\right]^{B_2} = \left[I_{B_2}^{B_2}\{1,1\}\right]^{B_2} \left[\frac{dp_2^{B_2 E}}{dt}\right]^{B_2} \tag{2b}$$

$$\begin{bmatrix} \dot{p}_2 \\ \dot{p}_1 \\ \dot{q} \\ \dot{r} \end{bmatrix} = \begin{bmatrix} I_{x_2}^{-1} & 0 & 0 & 0 \\ 0 & \tilde{I}_{x_1}^{-1} & 0 & 0 \\ 0 & 0 & \tilde{I}_t^{-1} & 0 \\ 0 & 0 & 0 & \tilde{I}_t^{-1} \end{bmatrix} \left(\begin{bmatrix} 0 & 0 & 0 & 0 \\ 0 & 0 & r & -q \\ 0 & -r & 0 & -r\tan\theta \\ 0 & q & r\tan\theta & 0 \end{bmatrix} \begin{bmatrix} I_{x_2} & 0 & 0 & 0 \\ 0 & \tilde{I}_{x_1} & 0 & 0 \\ 0 & 0 & \tilde{I}_t & 0 \\ 0 & 0 & 0 & \tilde{I}_t \end{bmatrix} \begin{bmatrix} p_2 \\ p_1 \\ q \\ r \end{bmatrix} + \begin{bmatrix} L_2 \\ L_1 \\ M \\ N \end{bmatrix} \right) \tag{2c}$$

The Euler attitude dynamic equations (2a)-(2b) represent, in tensor form, the attitude of the main body and the fuze of the projectile respectively [12]. The fuze attitude equation is only made of the roll motion. For the main body, the computation of the effective moment of inertia $\left[\tilde{I}_B^{B_{12}}\right]^{B'_1}$ is detailed in a previous publication [13]. $\left[\omega^{B_1 E}\right]^{B'_1} = [p_1 \quad q \quad r]^\top$ is the angular velocity vector of the main body and $\left[m_{B_1}\right]^{B'_1} = [L_1 \quad M \quad N]^\top$ is the external sum of moments applied on the main body of the projectile. In another part, p_2 is the spin rate of the fuze, $\left[I_{B_2}^{B_2}\right]^{B_2}$ is the MoI of the fuse part and $\left[m_{B_2}\{1,1\}\right]^{B_2} = L_2$ is the external roll moment applied on the fuze. The equation (2c) summarizes the attitude dynamic equation of both part in matrix form.

C. Translation and Attitude Kinematics

The translation kinematics equation expresses the velocity vector of the projectile center of mass B in the local frame coordinate system $]^L$ using a change of coordinate system by the transformation matrix $[T]^{B'_1 L}$. Then, by integrating $\left[v_B^E\right]^L$ the position vector $[s_{BE}]^L = [x \quad y \quad z]^\top$ is obtained. The transformation matrix is calculated from the Euler angles ϕ_1, θ, ψ resulting from Eq. (5)

$$\left[v_B^E\right]^L = \left[\overline{T}\right]^{B'_1 L} \left[v_B^E\right]^{B'_1} \tag{3a}$$

$$\begin{bmatrix} \dot{x} \\ \dot{y} \\ \dot{z} \end{bmatrix} = \begin{bmatrix} \cos\psi\cos\theta & -\sin\psi & \cos\psi\sin\theta \\ \sin\psi\cos\theta & \cos\psi & \sin\psi\sin\theta \\ -\sin\theta & 0 & \cos\theta \end{bmatrix} \begin{bmatrix} u \\ v \\ w \end{bmatrix} \tag{3b}$$

The Euler angles from the projectile main body $[\phi_1 \quad \theta \quad \psi]^\top$ are calculated by integrating the Directive Cosine Matrix (DCM), it may be notice that a singularity is present during the computation of Eq. (5) at $\theta = \frac{\pi}{2}$ and $\psi = \frac{\pi}{2}$ but this conditions exceeds the flight envelope. Because of the fixed null roll of the BFR frame, ϕ_1 and ϕ_2 can't be

3

determined with $[T]^{B_1'L}$. The fuse roll angle ϕ_2 and the main body roll angle ϕ_1 are directly integrated from the attitude dynamics.

$$\frac{\mathrm{d}[T]^{B_1'L}}{\mathrm{d}t} = \left[\overline{\Omega}^{B_1E}\right]^{B_1'} [T]^{B_1'L} \tag{4a}$$

$$[T]^{B_1'L} = \begin{bmatrix} \cos\psi\cos\theta & \sin\psi\cos\theta & -\sin\theta \\ -\sin\psi & \cos\psi & 0 \\ \sin\psi\sin\theta & \sin\psi\sin\theta & \cos\theta \end{bmatrix} \tag{4b}$$

$$\dot{\phi}_2 = p_2 + r\tan\theta \tag{5a}$$

$$\dot{\phi}_1 = p_1 + r\tan\theta \tag{5b}$$

$$\theta = -\arcsin\left(T^{B_1'L}\{1,3\}\right) \tag{5c}$$

$$\psi = -\arctan\left(\frac{T^{B_1'L}\{2,1\}}{T^{B_1'L}\{2,2\}}\right) \tag{5d}$$

D. Forces and Moments

During its flight, the projectile is subjected to the gravity force (G), and aerodynamic actions. The resultant forces and moments applied on the projectile are mostly due to drag and lift (P), damping (D) and Magnus effect (M) which creates an important lateral deviation of the trajectory due to the high spin rate of the projectile. In addition, the four embedded canards on the fuze create control forces and moments (C), influencing the projectile motions. Finally, mechanical friction between the fuze and the main body produces a moment L_f reducing the spin rate of the main body and increasing the spin rate of the fuze. Equation (7) is the vector representation of the external forces and moments tensor equations (6). Where S is the projectile reference area and d is the caliber. C_A, $C_{N\alpha}$, C_{Yp_α}, C_{N_q}, $C_{m\delta}$, C_{m_α}, $C_{n_{p_\alpha}}$, C_{l_p}, C_{m_q}, C_{l_δ}, C_{m_δ} are the aerodynamic coefficients. The flight parameters including, the airspeed V, the aerodynamic angles $\begin{bmatrix} \alpha & \beta \end{bmatrix}^\top$ and the mach number $\mathcal{M}$ are defined by Eq. (8d).

$$\left[f_B^{12}\right]^{B_1'} = \left[f_B^P\right]^{B_1'} + \left[f_B^M\right]^{B_1'} + \left[f_B^D\right]^{B_1'} + \left[f_B^C\right]^{B_1'} + \left[f_B^G\right]^{B_1'} \tag{6a}$$

$$\left[m_B^{12}\right]^{B_{1'2}} = \left[m_B^P\right]^{B_{1'2}} + \left[m_B^M\right]^{B_{1'2}} + \left[m_B^D\right]^{B_{1'2}} + \left[m_B^C\right]^{B_{1'2}} + \left[m_B^F\right]^{B_{1'2}} \tag{6b}$$

$$\begin{bmatrix} X \\ Y \\ Z \end{bmatrix} = \bar{q}S\left(\begin{bmatrix} -C_A \\ -C_{N_\alpha}\sin\beta \\ -C_{N_\alpha}\sin\alpha\cos\beta \end{bmatrix} + \frac{p_1 d}{2V}\begin{bmatrix} 0 \\ C_{Yp_\alpha}\sin\alpha\cos\beta \\ -C_{Yp_\alpha}\sin\beta \end{bmatrix} + \frac{d}{2V}\begin{bmatrix} 0 \\ C_{N_q}r \\ -C_{N_q}q \end{bmatrix} + \begin{bmatrix} 0 \\ C_{N_\delta}(\delta_r - \beta) \\ C_{N_\delta}(-\delta_q - \alpha) \end{bmatrix}\right) + mg\begin{bmatrix} -\sin\theta \\ 0 \\ \cos\theta \end{bmatrix} \tag{7a}$$

$$\begin{bmatrix} L_2 \\ L_1 \\ M \\ N \end{bmatrix} = \bar{q}Sd\left(\begin{bmatrix} 0 \\ 0 \\ C_{m_\alpha}\sin\alpha\cos\beta \\ -C_{m_\alpha}\sin\beta \end{bmatrix} + \frac{P_1 d}{2V}\begin{bmatrix} 0 \\ 0 \\ C_{n_{p_\alpha}}\sin\beta \\ -C_{n_{p_\alpha}}\sin\alpha\cos\beta \end{bmatrix} + \frac{d}{2V}\begin{bmatrix} 0 \\ C_{l_p}p_1 \\ C_{m_q}q \\ -C_{m_q}r \end{bmatrix} + \begin{bmatrix} C_{l_\delta}\delta_p \\ 0 \\ C_{m_\delta}(\delta_q + \alpha) \\ C_{m_\delta}(\delta_r - \beta) \end{bmatrix}\right) + \begin{bmatrix} L_f \\ -L_f \\ 0 \\ 0 \end{bmatrix} \tag{7b}$$

$$L_f = \bar{q}SdC_A\mathrm{sgn}\,(p_1 - p_2)\,(K_s + K_v)\,|p_1 - p_2| \tag{7c}$$

$$V = \sqrt{u^2 + v^2 + w^2} \tag{8a}$$

$$\alpha = \arctan\left(\frac{w}{u}\right) \tag{8b}$$

$$\beta = \arctan\left(\frac{v}{\sqrt{u^2 + w^2}}\right) \tag{8c}$$

$$\mathcal{M} = \frac{V}{a} \tag{8d}$$

4

E. Control Allocation and Actuator Model

The relation from Eq. (9a) gives the correspondence between the signal given to each physical servomotors moving the canards $[\delta_r] = [\,\delta_1 \quad \delta_2 \quad \delta_3 \quad \delta_4\,]^\top$ and the virtual roll, pitch and yaw signals given by the autopilot $[\delta_v] = [\,\delta_p \quad \delta_q \quad \delta_r\,]^\top$. From the control allocation matrix $[T]^{VR}$ it can be seen that the four canards have a contribution to the roll command δ_p, only the canards on the yaw plane $[\,\delta_1 \quad \delta_3\,]^\top$ affects the pitch commands δ_q and only the canards on the pitch plane $[\,\delta_2 \quad \delta_4\,]^\top$ affect the yaw command δ_r .

$$[\delta_v]^{B_1'} = \left[\overline{T}\right]^{B_2 B_1'} [T]^{VR} [\delta_r]^{B_2} \tag{9a}$$

$$[T]^{VR} = \begin{bmatrix} -1/4 & 1/4 & 1/4 & -1/4 \\ 1/2 & 0 & 1/2 & 0 \\ 0 & 1/2 & 0 & 1/2 \end{bmatrix} \tag{9b}$$

$$[T]^{B_2 B_1'} = \begin{bmatrix} 1 & 0 & 0 \\ 0 & \cos\phi_2 & \sin\phi_2 \\ 0 & -\sin\phi_2 & \cos\phi_2 \end{bmatrix} \tag{9c}$$

The dynamics of each canard is modeled by a second order transfer function and is taken into account in the design and the simulations. The modeling of actuators dynamic is important because INDI control laws give an incremental control signal which must be added to the last time-step actuators position. Actuators speed therefore affects INDI performance and stability.

$$G_\delta(s) = \frac{\omega_\delta^2}{s^2 + 2\xi_\delta \omega_\delta s + \omega_\delta^2} \tag{10}$$

F. Sensor Model

The roll decoupled fuze embeds all necessary sensors to measure the states of the systems: gyroscope, magnetometers, GNSS and IMU. In this paper, the dynamic of the sensors is not considered and each one is supposed to be instantaneous and unbiased. The expressions of the load factors measured by the IMU is defined by Eq. (11).

$$\begin{bmatrix} n_x \\ n_y \\ n_z \end{bmatrix} = \frac{1}{mg} \left(\begin{bmatrix} X \\ Y \\ Z \end{bmatrix} - mg \begin{bmatrix} -\sin\theta \\ 0 \\ \cos\theta \end{bmatrix} \right) \tag{11}$$

III. INDI Baseline Autopilot

The flight of the presented dual-spin projectile is decomposed into multiple phases as shown in Fig. 2. First, from the launch to the apogee where $t < t_3$ the projectile is completing its ascension, no control is applied on the lateral channels thus the projectile stays in ballistic behavior. At the same time, because of the friction between the main body and the fuze, the roll rate of the fuse increases. In the second phase, when $t_2 > t > t_1$ all the canards are put on maximum deflections in order to reduce the roll rate of the fuse until $p_2 < p_{2_0}$. After p_2 is sufficiently reduced, the roll autopilot, detailed in Section III.A is launched to maintain a fixed roll angle given by the guidance law to the fuze. During the descent of the projectile when $t > t_3$, the trajectory is controlled by a cascaded INDI autopilot structure based on time-scale separation. The fast and slow inversion stages are detailed in Section III.B.1and Section III.B.2 respectively.

The design procedure for the roll autopilot and load factors autopilot are quite similar to a previous publication [14], however, the load factors dynamics is directly used in the inversion without need for measurement on the aerodynamic angles. First, the expression of the INDI command is from the general equation (12), then the quality of inversion of discrete time INDI with real actuators is verified analytically. A discrete model of the inverted plant is obtained which is then converted into an equivalent continuous time model using inverted Tustin's bilinear transform. This continuous-time linear model is used to design the outer loop linear controller following the Modified Continuous Design method [15] associated to $\mathcal{H}_\infty$ robust control theory. Finally, the resulting controller is validated in nonlinear simulations.

$$\boldsymbol{u}_k = \boldsymbol{u}_{k-1} + G^{-1}\left(\boldsymbol{v}_k - \frac{\boldsymbol{x}_k - \boldsymbol{x}_{k-1}}{T}\right) \tag{12}$$
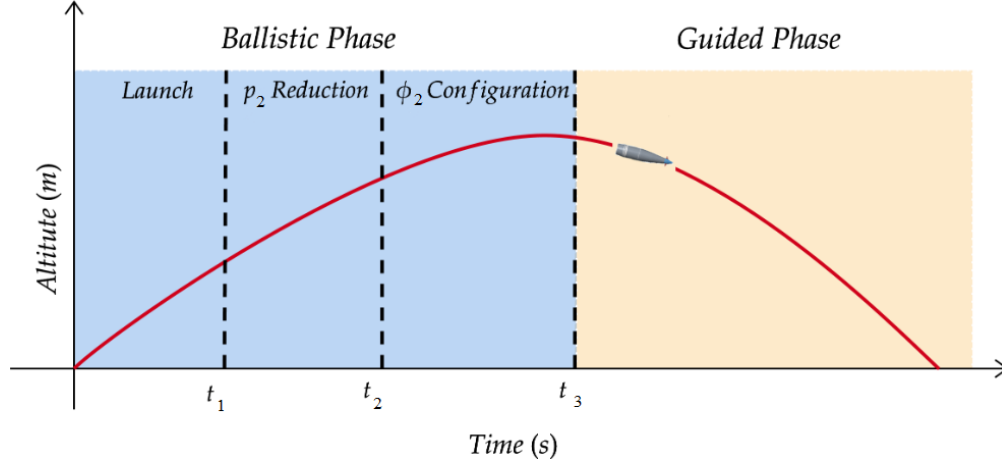
5

Fig. 2   Flight phases of the projectile

INDI theory is based on the reformulation of the system dynamic equations in an incremental form using first-order Taylor series approximation (27). INDI autopilots are structured in an inner/outer loop configuration illustrated by Fig. 3. The inner loop inverts the plant using Eq. (12), where T is the sampling period, x are the states, u is the control signal and v is the pseudo-control variable defined by the outer loop controller. G is the control effectiveness matrix calculated with Eq. (13).

$$G = \frac{\partial \dot{x}(x, u)}{\partial u} \tag{13}$$

A. Roll autopilot
The roll dynamics equations are recalled by Eq. (14). If the friction moment and the motion of the BFR frame are considered as external disturbances, the system is linear and can be described with a state space representation.

$$\begin{cases} \dot{\phi}_2 = p_2 + r \tan\theta \\ \dot{p}_2 = I_{x_2}^{-1} L_2 \end{cases} \tag{14}$$

$$\begin{bmatrix} \dot{\phi}_2 \\ \dot{p}_2 \end{bmatrix} = \begin{bmatrix} 0 & 1 \\ 0 & 0 \end{bmatrix} \begin{bmatrix} \phi_2 \\ p_2 \end{bmatrix} + \begin{bmatrix} 0 \\ I_{x_2}^{-1} L_c \end{bmatrix} \delta_p + \begin{bmatrix} r \tan\theta \\ L_f \end{bmatrix} \tag{15a}$$

$$\begin{bmatrix} y_1 \\ y_2 \end{bmatrix} = \begin{bmatrix} 0 & 1 \\ 1 & 0 \end{bmatrix} \begin{bmatrix} \phi_2 \\ p_2 \end{bmatrix} \tag{15b}$$

At this point a clarification must be made, as the relation between ϕ_2 and p_2 is already a simple integrator, INDI is used to invert $\dot{p}_2$ dynamics. Afterward, in the ideal case, the input-output map from δ_p to ϕ_2 will be a double integrator.
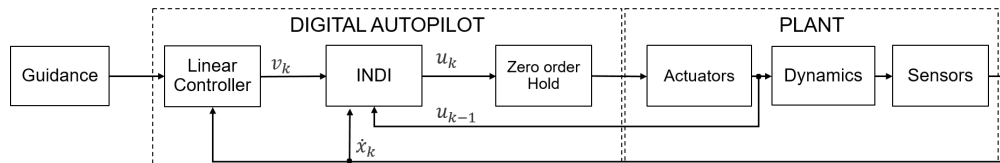

Fig. 3   INDI autopilot architecture

6

The INDI command for the roll channel is obtained from Eq. (14) applied to the roll dynamics.

$$\delta_p[k] = \delta_p[k-1] + G^{-1}\left(v[k] - \frac{p_2[k] - p_2[k-1]}{T}\right) \tag{16a}$$

$$G = \frac{\partial \dot{p}_2}{\partial \delta_p} = I_{x_2}^{-1}\overline{q}SdC_{l_\delta} \tag{16b}$$

All the parameters involved in G are strictly positive for all the flight envelope then G is always invertible. The INDI command is summarized by Eq. (17).

$$\delta_p[k] = \delta_p[k-1] + \frac{I_{x_2}}{\overline{q}SdC_{l_\delta}}\left(v[k] - \frac{p_2[k] - p_2[k-1]}{T}\right) \tag{17}$$

It can be proven analytically that in absence of delays on measurement and with perfects actuators the inversion is valid in discrete time and obtain $\dot{p}_2 = v$ by injecting Eq. (17) in Eq. (14). For the sake of clarity and to avoid any confusion for the reader between the continuous roll acceleration $\dot{p}_2$ and its discrete expression with the INDI command, in the following analytical development, the discrete counter part of $\dot{p}_2$ is noted $\tilde{p}_2$. However, in the presented system, the actuators are modeled by $G_\delta(s)$ and therefore by replacing $\delta_p(z)$ by $\mathcal{Z}\{G_\delta(s)\}\delta_p(z)$ in Eq. (18), the real inversion is obtained in Eq (18).

$$\dot{p}_2 = GG_\delta(s)\delta_p(s)$$

$$\Leftrightarrow \tilde{p}_2 = G\mathcal{Z}\{G_\delta(s)\}\delta_p(z) = G\mathcal{Z}\{G_\delta(s)\}\left(\mathcal{Z}\{G_\delta(s)\}z^{-1}\delta_p(z) + G^{-1}\left(v - \frac{p_2 - z^{-1}p_2}{T}\right)\right)$$

$$\Leftrightarrow \tilde{p}_2 = z^{-1}\mathcal{Z}\{G_\delta(s)\}^2\tilde{p}_2 + \mathcal{Z}\{G_\delta(s)\}v - \mathcal{Z}\{G_\delta(s)\}\tilde{p}_2$$

$$\Leftrightarrow \tilde{p}_2\left(1 - z^{-1}\mathcal{Z}\{G_\delta(s)\}^2 + \mathcal{Z}\{G_\delta(s)\}\right) = \mathcal{Z}\{G_\delta(s)\}v$$

$$\Leftrightarrow \tilde{p}_2 = \frac{1}{\mathcal{Z}\{G_\delta(s)\}^{-1} - z^{-1}\mathcal{Z}\{G_\delta(s)\} + 1}v \tag{18}$$

It can be verified that with perfect actuators and continuous time ($G_\delta(s) = 1$ and $z = 1$ in Eq. (18)) the inversion is perfect ($\tilde{p}_2 = v$). The figure 4 compares the modeling of the inverted model described by Eq. (18), the real inversion in simulation, and a perfect inversion in discrete time (chain of discrete-time integrators). The inversion is very close to a double integrator for the roll channel, the INDI inner-loop transfer function can be approximated by a double integrator for the design of the external controller. $\mathcal{H}_\infty$ robust control theory associated with Modified Continuous Design was used to tune, in continuous time the gains of the controller, while taking into account digital implementation constraints like Zero Order Hold and computational delay. In the roll external controller design model in Fig. 5 $G_{\text{ZOH}}(s)$ and $G_d(s)$ are Pade approximation of Zero Order Hold and computational delay transfer function respectively and $G_r(s)$ is the second-order reference model with $\omega_r = 17.1$ rad/s and $\xi_r = 0.78$. Each filter $W_r(s), W_{S_o}(s), W_{KS}(s)$ [16] is used to defined the $\mathcal{H}_\infty$ optimization problem which was solved with Matlab `systune`.
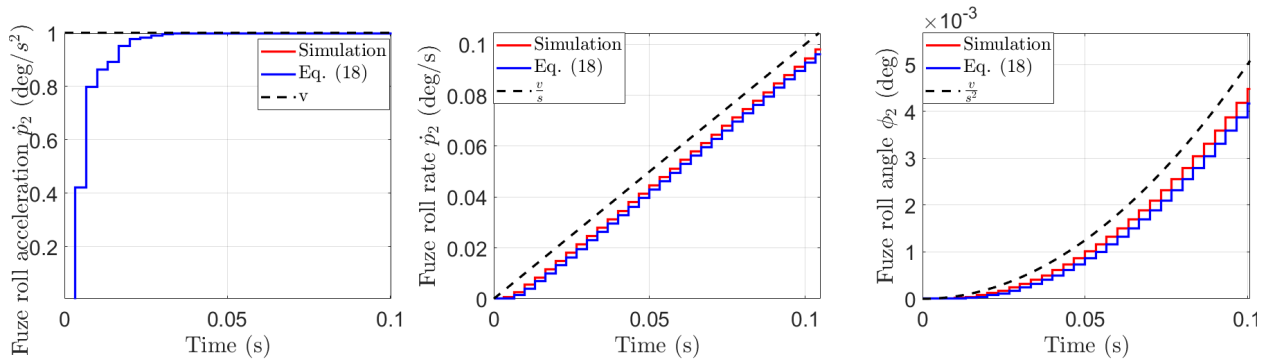

Fig. 4   Modeling of the INDI inversion error for the roll channel
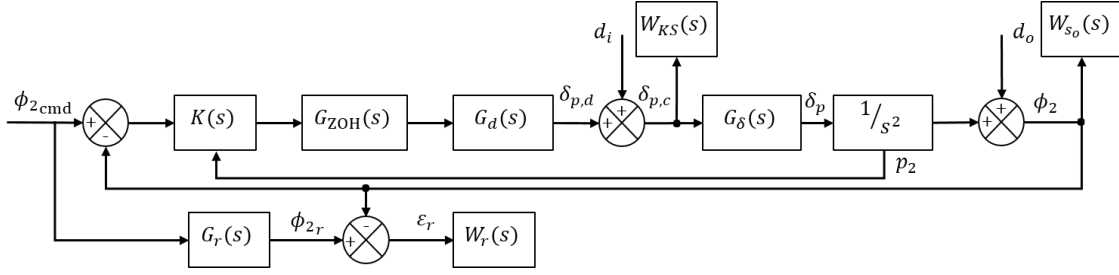
7

Fig. 5   Roll external controller design model

B. Load Factor Autopilot

The projectile trajectory is controlled by the mean of the lateral desired load factors $[n_{z,c} \quad n_{y,c}]^\top$ computed by the embedded Zero Effort Miss guidance law [17]. To ensure that the real load factors are following the guidance law, a two cascaded INDI autopilot structure illustrated by Fig. 6 was used under the assumption of time-scale separation between two identified fast and slow dynamics. More precisely, the lateral rates of the projectile $[q \quad r]^\top$ are considered to vary much faster than the load factors. This time-scale separation scheme has been proven valid and is presented by [18]. The following subsections details the design of each stage of the autopilot.

1. Fast Dynamic controller

The fast dynamic controller decouples and controls the lateral channels $[q \quad r]^\top$ of the projectile using the lateral control inputs $[\delta_q \quad \delta_r]^\top$. The nonlinear MIMO system to be controlled is summarized by Eq. (19).

$$\begin{cases} \dot{q} = -\frac{I_{x_1}}{I_t} p_1 r - r^2 \tan\theta + \frac{M}{I_t} \\ \dot{r} = \frac{I_{x_1}}{I_t} p_1 q - qr \tan\theta + \frac{N}{I_t} \end{cases} \tag{19}$$

The design of the fast dynamic INDI autopilot is not explained in details in this paper because it has already been involved in previous work [13] and therefore doesn't contribute to the novelty of the paper. However the main equations are recalled and additional analytical analysis on INDI inversion is added in this paper. The control effectiveness matrix G and the INDI command are obtained from Eq. (12) and Eq. (13) applied to the lateral channels equations Eq. (19).

$$G = \begin{bmatrix} \frac{\partial \dot{q}}{\partial \delta_q} & \frac{\partial \dot{q}}{\partial \delta_r} \\ \frac{\partial \dot{r}}{\partial \delta_q} & \frac{\partial \dot{r}}{\partial \delta_r} \end{bmatrix} = \begin{bmatrix} \left(\frac{\bar{q}Sd}{\bar{I}_t}\right) C_{m_\delta} & 0 \\ 0 & \left(\frac{\bar{q}Sd}{\bar{I}_t}\right) C_{m_\delta} \end{bmatrix} \tag{20}$$

$$\begin{bmatrix} \delta_q[k] \\ \delta_r[k] \end{bmatrix} = \begin{bmatrix} \delta_q[k-1] \\ \delta_r[k-1] \end{bmatrix} + \begin{bmatrix} \frac{I_t}{\bar{q}SdC_{m_\delta}} & 0 \\ 0 & \frac{\bar{I}_t}{\bar{q}SdC_{m_\delta}} \end{bmatrix} \begin{bmatrix} v_q[k] - \frac{q[k]-q[k-1]}{T} \\ v_r[k] - \frac{r[k]-r[k-1]}{T} \end{bmatrix} \tag{21}$$

Similarly to the notation introduced in Eq. (18), the discrete counter part of $\dot{q}$ and $\dot{r}$ are noted $\tilde{q}$ and $\tilde{r}$ respectively. The same analysis as for the roll is conducted, the objective is to verify that the INDI inner-loop inversion in discrete-time
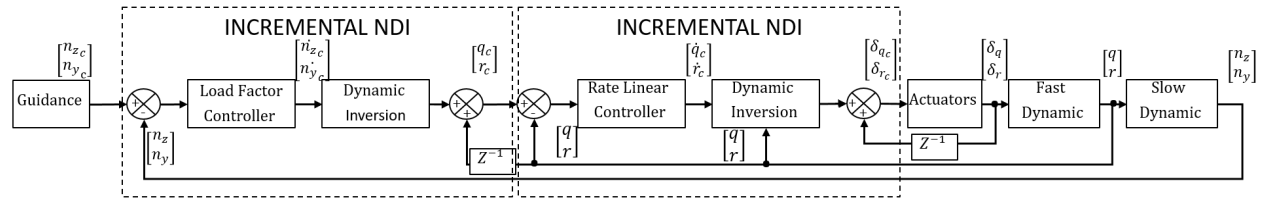

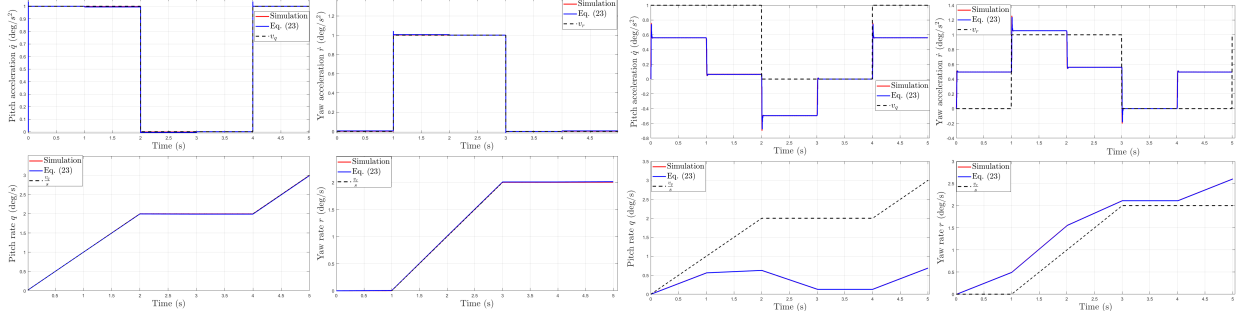**Fig. 6   Load factor autopilot architecture**

8

Fig. 7   Modeling of the INDI inversion error for the lateral channels

and with non perfect actuators is valid: $[\tilde{q} \quad \tilde{r}]^\top = [v_q \quad v_r]^\top$.

$$\begin{bmatrix} \dot{q} \\ \dot{r} \end{bmatrix} = \begin{bmatrix} -\left(I_{x_1}I_t^{-1}p_1 + r\tan\theta\right)r \\ \left(I_{x_1}I_t^{-1}p_1 + r\tan\theta\right)q \end{bmatrix} + \frac{\bar{q}Sd}{I_t}\left(\begin{bmatrix} C_{m_\alpha}\sin\alpha\cos\beta \\ -C_{m_\alpha}\sin\beta \end{bmatrix} + \frac{P_1 d}{2V}\begin{bmatrix} C_{n_{p_\alpha}}\sin\beta \\ -C_{n_{p_\alpha}}\sin\alpha\cos\beta \end{bmatrix} + \frac{d}{2V}\begin{bmatrix} C_{m_q}q \\ -C_{m_q}r \end{bmatrix} + \begin{bmatrix} C_{m_\delta}(\delta_q + \alpha) \\ C_{m_\delta}(\delta_r - \beta) \end{bmatrix}\right)$$

$$\Leftrightarrow \begin{bmatrix} \tilde{q} \\ \tilde{r} \end{bmatrix} = \begin{bmatrix} -\left(I_{x_1}I_t^{-1}p_1 + r\tan\theta\right)r \\ \left(I_{x_1}I_t^{-1}p_1 + r\tan\theta\right)q \end{bmatrix} + \frac{\bar{q}Sd}{I_t}\left(\begin{bmatrix} C_{m_\alpha}\sin\alpha\cos\beta \\ -C_{m_\alpha}\sin\beta \end{bmatrix} + \frac{P_1 d}{2V}\begin{bmatrix} C_{n_{p_\alpha}}\sin\beta \\ -C_{n_{p_\alpha}}\sin\alpha\cos\beta \end{bmatrix} + \frac{d}{2V}\begin{bmatrix} C_{m_q}q \\ -C_{m_q}r \end{bmatrix}\right.$$

$$\left. + \begin{bmatrix} C_{m_\delta}\mathcal{Z}\{G_\delta(s)\}\left(z^{-1}\delta_q + \frac{\bar{I}_t}{\bar{q}SdC_{m_\delta}}\left(v_q - \frac{q - z^{-1}q}{T}\right) + \alpha\right) \\ C_{m_\delta}\mathcal{Z}\{G_\delta(s)\}\left(z^{-1}\delta_r + \frac{\bar{I}_t}{\bar{q}SdC_{m_\delta}}\left(v_r - \frac{r - z^{-1}r}{T}\right) - \beta\right) \end{bmatrix}\right)$$

$$\Leftrightarrow \begin{bmatrix} \tilde{q} \\ \tilde{r} \end{bmatrix} = \begin{bmatrix} \tilde{q} \\ \tilde{r} \end{bmatrix} - \left(1 - z^{-1}\mathcal{Z}\{G_\delta(s)\}\right)G\begin{bmatrix} \delta_q \\ \delta_r \end{bmatrix} + \mathcal{Z}\{G_\delta(s)\}\begin{bmatrix} v_q - \frac{q}{T}(1 - z^{-1}) \\ v_r - \frac{r}{T}(1 - z^{-1}) \end{bmatrix}$$

$$\Leftrightarrow \begin{bmatrix} \tilde{q} \\ \tilde{r} \end{bmatrix} = \begin{bmatrix} \tilde{q} \\ \tilde{r} \end{bmatrix} - \left(1 - z^{-1}\mathcal{Z}\{G_\delta(s)\}\right)G\begin{bmatrix} \delta_q \\ \delta_r \end{bmatrix} + \mathcal{Z}\{G_\delta(s)\}\begin{bmatrix} v_q - \frac{\tilde{q}}{T}\frac{Tz}{z-1}\frac{z-1}{z} \\ v_r - \frac{\tilde{r}}{T}\frac{Tz}{z-1}\frac{z-1}{z} \end{bmatrix}$$

$$\Leftrightarrow \begin{bmatrix} \tilde{q} \\ \tilde{r} \end{bmatrix} = \left(\frac{\mathcal{Z}\{G_\delta(s)\} - z}{z\mathcal{Z}\{G_\delta(s)\}}\right)\begin{bmatrix} \frac{\bar{q}SdC_{m_\delta}}{\bar{I}_t} & 0 \\ 0 & \frac{\bar{q}SdC_{m_\delta}}{\bar{I}_t} \end{bmatrix}\begin{bmatrix} \delta_q \\ \delta_r \end{bmatrix} + \begin{bmatrix} v_q \\ v_r \end{bmatrix} \tag{22}$$

In the same way as for the roll channel, the analytical expression of the real inversion enlightens the impact of sampling frequency and actuators speed on the INDI inversion. Fig. 7 shows the comparison between the simulation model of the INDI inversion and the analytical expression of Eq. (22). The analytical model matches very well the INDI simulation and it can be checked that with perfect actuators and with continuous time, the inversion is perfect. The sampling frequency has a direct impact on decoupling capacities and therefore a full order $\mathcal{H}_\infty$ controller was designed to handle non-perfect inversion, the design has been detailed in [13] with time domain specifications sets to a settling time of 0.3 s and a 2% max overshoot.

2. Slow Dynamic controller

The slow dynamics stage of the load factor autopilot computes the desired lateral rates dynamic $[\dot{q}_c \quad \dot{r}_c]^\top$ from the desired load factors $[n_{y,c} \quad n_{z,c}]^\top$. To obtain the analytical expression of the INDI inversion, $[n_y \quad n_z]^\top$ must be time-differentiated.

$$\begin{bmatrix} \dot{n}_y \\ \dot{n}_z \end{bmatrix} = \frac{1}{mg}\left(\begin{bmatrix} \frac{dY}{dt} \\ \frac{d(Z - \cos\theta)}{dt} \end{bmatrix}\right) \tag{23}$$

In the nonlinear MIMO system described by Eq. (23), the states are the load factors $[n_z \quad n_y]^\top$ and the control inputs are $[q \quad r]^\top$, thus the control effectiveness matrix of this system G is then obtained with Eq. (25a). The computation of $[\dot{n}_y \quad \dot{n}_z]$ and G involves a lot of time varying parameters and states therefore to avoid any mistakes Matlab symbolic Toolbox was used. The influence of the lateral rates does not completely appear in the expression of Eq. (23), but it can be revealed by replacing $\dot{\alpha}$ and $\dot{\beta}$ by their analytical expression obtained from the reformulation of Eq. (1b) using a
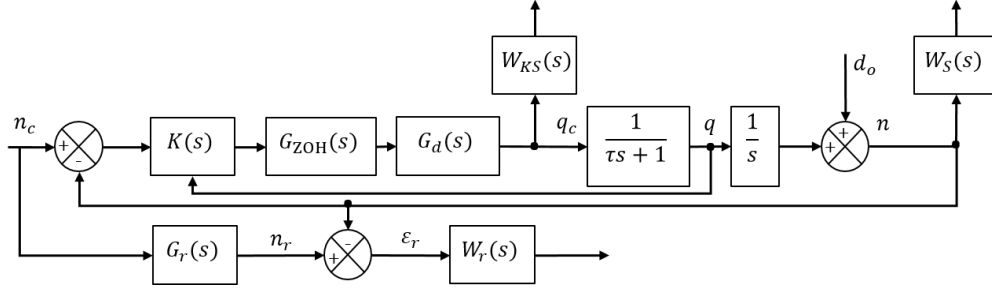
9

Fig. 8   Load factor external controller design model

change of variable [2].

$$
\begin{cases}
\dot{\alpha} = q + r \left(\cos\alpha \tan\theta - \sin\alpha \right) \tan\beta \frac{1}{mV} \left(\frac{-\sin\alpha}{\cos\beta} X + \frac{\cos\alpha}{\cos\beta} Z \right) \\
\dot{\beta} = -r \left(\cos\alpha + \sin\alpha \tan\theta \right) + \frac{1}{mV} \left(\cos\alpha \sin\beta X + \cos\beta Y - \sin\alpha \sin\beta Z \right)
\end{cases}
\tag{24}
$$

The analytical analysis of the slow dynamic inversion in discrete time hasn't been conducted yet but simulation results show the satisfactory decoupling and linearization of the slow dynamic controller. As for the dynamic inversion applied to the roll and lateral channels, the invertibility of G was verified for all the flight envelope.

$$
\begin{bmatrix} \frac{\partial \dot{n}_y}{\partial q} & \frac{\partial \dot{n}_y}{\partial r} \\ \frac{\partial \dot{n}_z}{\partial q} & \frac{\partial \dot{n}_z}{\partial r} \end{bmatrix} = \frac{\bar{q}S}{gm} \begin{bmatrix} -C_{N_\delta} - C_{N_\alpha} & (\tan\theta - \alpha)\beta \left(C_{N_\delta} - C_{N_\alpha} \right) - (\tan\theta\alpha + 1)\left(\frac{p_1 d}{2V} C_{Y_{P_\alpha}} \right) \\ \left(\frac{p_1 d}{2V} \right) C_{Y_{P_\alpha}} & (\tan\theta\alpha + 1)\left(C_{N_\delta} + C_{N_\alpha} \right) + (\tan\theta - \alpha)\left(\frac{p_1 d}{2V} \right) C_{Y_{P_\alpha}} \beta \end{bmatrix}
\tag{25a}
$$

$$
\begin{bmatrix} q_c[k] \\ r_c[k] \end{bmatrix} = \begin{bmatrix} q_c[k-1] \\ r_c[k-1] \end{bmatrix} + G^{-1} \begin{bmatrix} v_{n_z}[k] - \frac{n_z[k] - n_z[k-1]}{T} \\ v_{n_y}[k] - \frac{n_y[k] - n_y[k-1]}{T} \end{bmatrix}
\tag{25b}
$$

The decoupling of n_y and n_z by the INDI slow dynamic stage allows to reduce the external controller design model to a SISO system. The same design methodology as for the roll was employed, where Matlab `systune` was used to tune the external controller. The design model shown in Fig. 8 includes the closed-loop fast dynamics modeled as a first order system with $\tau = 0.07$. To ensure time scale separation between fast and slow dynamics, a 2% settling time of 1.5 s was imposed which is sufficiently slower compared to fast dynamics settling time of 0.3 s, a maximum overshoot of 2% is specified as well.

C. Nonlinear simulation results

The figures 9,10,11 show nonlinear simulations of the roll, lateral rates and load factors autopilots respectively. In Fig. 9, the fuze roll is oscillating due to the friction and the spin rate is reduced by putting the four canards into saturation at $t = 20$ s. Then for performance evaluation purposes, the fuze roll angle is stabilized between 0 and 90 degrees. It can be observed that the control input is scaled to the flight point thanks to dynamic inversion. Around apogee, the airspeed is low thus the system has less control authority and therefore the control input is at its peak. In Fig. 10, the performance of the lateral channels controller launched at $t = 30$s is not homogeneous through the trajectory, because the real inversion Eq. (22) is not perfect. More precisely Eq. (22) reveals that with non perfects actuators the inverted model is still impacted of the flight point (flight parameters are presents in Eq. (22)). A single controller is therefore not sufficient for all the flight envelope. This issue is one of the motivation for an adaptive control augmentation and is addressed in Section IV.D. Thirdly, in Fig. 11, a satisfactory tracking of the desired load factors can be observed with the implementation of the cascaded INDI autopilot. Finally, full trajectory nonlinear simulation in Fig. 12 shows the capacity of the baseline autopilot coupled with a Zero Effort Miss guidance law to correct the ballistic dispersion and successfully reach the target under nominal conditions.
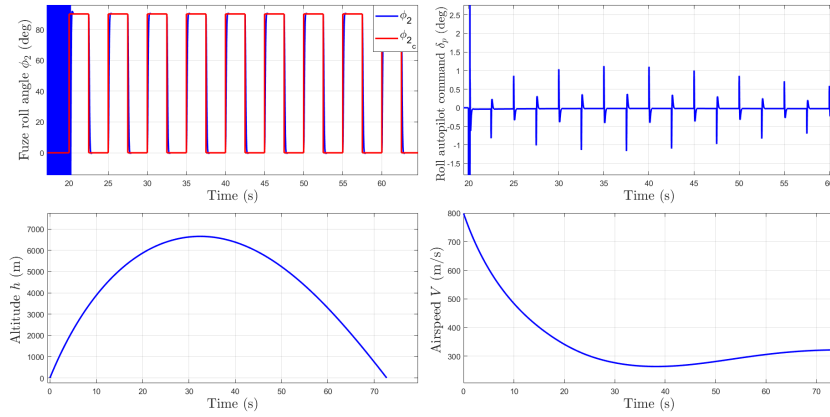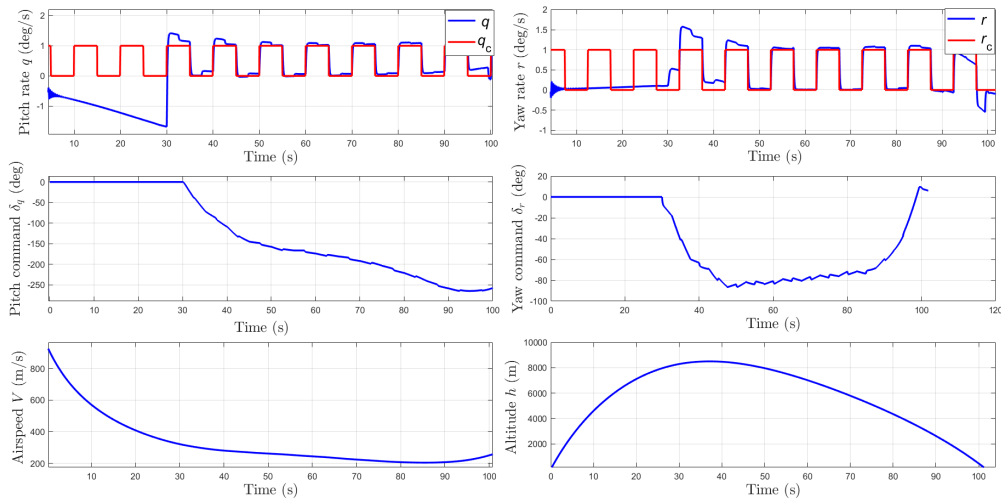
10

Fig. 9   Roll autopilot nonlinear simulation
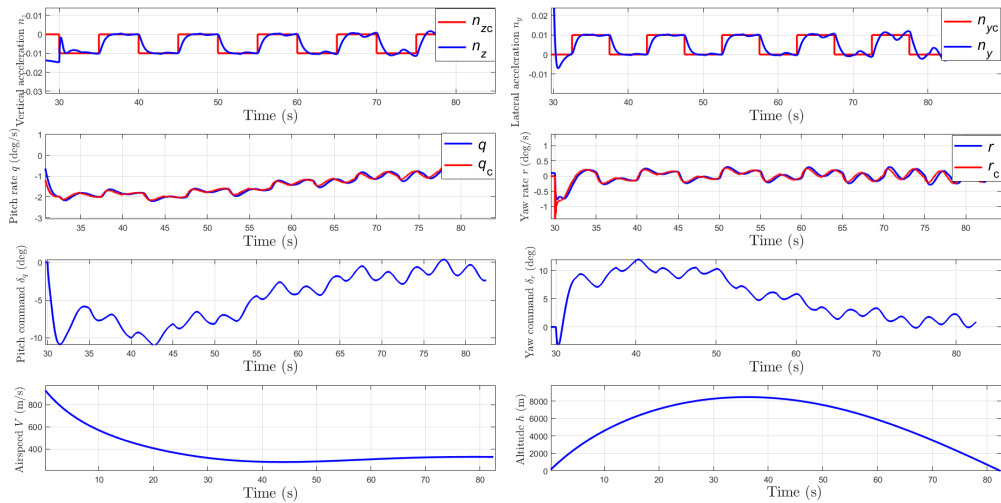

Fig. 10   Lateral channels autopilot nonlinear simulation

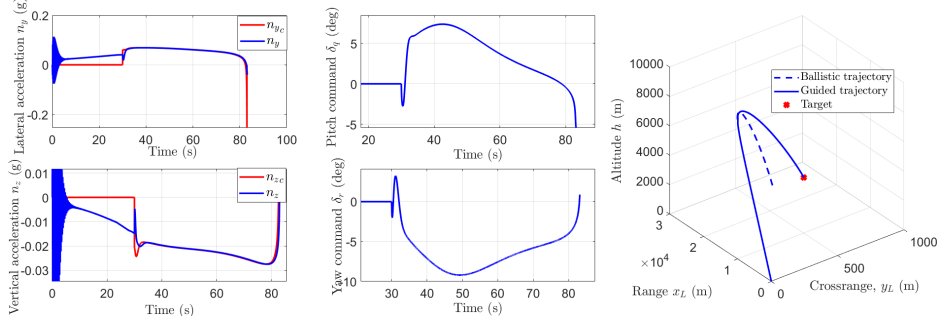**Fig. 11   Load factor autopilot nonlinear simulation**

Fig. 12   Guided trajectory simulation

IV. $\mathcal{L}_1$ Adaptive Augmentation

This section deals with the implementation of an $\mathcal{L}_1$ adaptive augmentation scheme for the INDI baseline autopilot designed in Section III. As a matter of fact, even if INDI is more robust to model mismatch than classical Nonlinear Dynamic Inversion because INDI uses only parameters related to control effectiveness, in this end a lot of parameters are involved in the inversion, like in Eq. (25a). Among these parameters, some are well known or reliably estimated like the projectile parameters $[S \quad d \quad m]^\top$ and others are subjected to important uncertainties like the aerodynamic coefficients. The estimation of these coefficients rely on expensive and time-consuming wind tunnel tests. Adaptive control can be a solution to counteract the effect on model mismatch on the autopilot and also correct the undesired effects of actuators speed and sampling frequency on INDI performance which is very significant for the lateral channels inversion.

The interest of the international scientific community for adaptive control has grown in the last few decades thanks to a lot of interesting results especially in the domain of aerospace [19, 20]. However, the beginnings of research in adaptive control date back to the 1950s with the development of adaptive autopilot for supersonic aircraft. An important step in adaptive control theory in the first publications from Whitaker and Osburn in 1958 and 1961 [21, 22] on a novel control architecture called Model Reference Adaptive Control(MRAC). In the 1980's, the work of Ioannou and Kokotovic [23] led to an improvement of the robustness and further analysis of the MRAC.

Model Reference Adaptive Control has nonetheless several issues that needs to be addressed. The main problem of MRAC is that to capture a large scale of uncertainties the adaptation gain must be high which could lead to output oscillation and reduce significantly the time delay margin. From this observation, $\mathcal{L}_1$ adaptive control proposes an alternative to MRAC where the adaptation is decoupled from robustness. In $\mathcal{L}_1$ adaptive control theory, the problem formulation is different than MRAC. In MRAC, the cancellation of uncertainties in the entire frequency domain is addressed. Whereas, the main assumption of $\mathcal{L}_1$-AC is that the controller is only able to cancel uncertainties in the bandwidth of the control channel [24]. The key point of $\mathcal{L}_1$-AC is the so-called underlying low-pass filter which decoupled adaptation or performance and robustness (time delay margin). $\mathcal{L}_1$ has been applied to several aerospace systems in simulation and flight tests [25–27] In the following subsection, the impact of uncertainties on INDI inversion is evaluated analytically, secondly, the $\mathcal{L}_1$ adaptive augmentation architecture used is presented, then the augmentation for the roll and the lateral channels INDI autopilot are detailed with nonlinear simulations results.

A. Parametric uncertainties effect on INDI performance

For the evaluation of the effect of parametric uncertainties on INDI in the general case, the inversion is considered perfect before the introduction of uncertainties in the system. Then the effect on real inversion will be detailed in the design of the adaptive augmentation of each channel. The starting point of INDI theory is to rewrite the dynamic equation the nonlinear system Eq. (26) in an incremental form using Taylor series approximation, resulting in Eq. (27).

$$\dot{x} = f(x, u) \tag{26}$$

$$\dot{x} \approx f(x_0, u_0) + \left.\frac{\mathrm{d}f(x, u)}{\mathrm{d}x}\right|_{x=x_0, u=u_0} (x - x_0) + \left.\frac{\mathrm{d}f(x, u)}{\mathrm{d}u}\right|_{x=x_0, u=u_0} (u - u_0) \tag{27}$$

$$\dot{x} = \dot{x}_0 + F\Delta x + G\Delta u \tag{28}$$

The main assumption of INDI theory is to consider time scale separation between the states and the actuators dynamics, more precisely the states are supposed to vary much slower than the actuator $\Delta x \ll \Delta u$. A simplified

12

approximation of the dynamics is obtained in Eq.(29) by neglecting $F\Delta\boldsymbol{x}$ in Eq. (28).

$$\dot{\boldsymbol{x}} = \dot{\boldsymbol{x}}_0 + G\Delta\boldsymbol{u} = \boldsymbol{v} \tag{29}$$

$$\Delta\boldsymbol{u} = G^{-1}(\boldsymbol{v} - \dot{\boldsymbol{x}}_0) \tag{30}$$

In the nominal case Eq. (30) inverts perfectly Eq. (29) and $\dot{\boldsymbol{x}} = \boldsymbol{v}$ is obtained. However, in the case of uncertainties the inversion is degraded.

$$G = G_n + \Delta G \tag{31a}$$

$$\dot{\boldsymbol{x}} = \dot{\boldsymbol{x}}_0 + (G_n + \Delta G)\, G_n^{-1}(\boldsymbol{v} - \dot{\boldsymbol{x}}_0)$$

$$= \boldsymbol{v} + \Delta G G_n^{-1}(\boldsymbol{v} - \dot{\boldsymbol{x}}_0) \tag{31b}$$

In Eq.32, G_n is the nominal value of the control effectiveness matrix and ΔG is the uncertainty component. If an adaptive augmentation is considered as in Eq. (32) then a perfect cancellation of all the uncertainties is obtained, however this control law is not implementable because it requires to know the uncertainties beforehand.

$$\Delta\boldsymbol{u} = \Delta\boldsymbol{u}_{\text{bl}} + \Delta\boldsymbol{u}_{\text{ad}}$$

$$\Delta\boldsymbol{u}_{\text{bl}} = G_n^{-1}(\boldsymbol{v} - \dot{\boldsymbol{x}}_0) \tag{32}$$

$$\Delta\boldsymbol{u}_{\text{ad}} = -\Delta G G_n^{-1}\Delta\boldsymbol{u}$$

B. $\mathcal{L}_1$ adaptive augmentation architecture

The purpose of this adaptive augmentation is to generate the incremental control signal $\Delta\boldsymbol{u}_{\text{ad}}$ that will cancel the error on dynamic inversion. The adaptive augmentation scheme used is shown in Fig. 13 and is similar to Bhardwaj et al. in [8] for the adaptive augmentation of an F-16 extend model. The $\mathcal{L}_1$ adaptive part is composed of three main blocks. First, the state predictor reproduces the output of the system taking into account the estimation of the uncertainties, the prediction error is then fed to the estimation law which calculates the value of the uncertainty represented by the parameter σ that will drive the prediction error to 0. Several approaches can considered for the adaptation law, based on projection [24] or piecewise-constant [28]. The estimated parameter $\hat{\sigma}$ is filtered by the low-pass filter $C(s)$ that will set the trade-off between performance and minimal time-delay margin. In the end, the adaptive incremental control law is :

$$\Delta\boldsymbol{u}_{\text{ad}} = -C(s)\hat{\sigma} \tag{33}$$

1. Output Predictor

The state predictor equation comes from the incremental form of the uncertain dynamic equation.

$$\dot{x} = \dot{x}_0 + (G_n + \Delta G)\, \Delta u$$

$$= \dot{x}_0 + G_n \left(\Delta u + G_n^{-1}\Delta G\Delta u\right)$$

$$= \dot{x}_0 + G_n \left(\Delta u + \sigma\right) \tag{34}$$
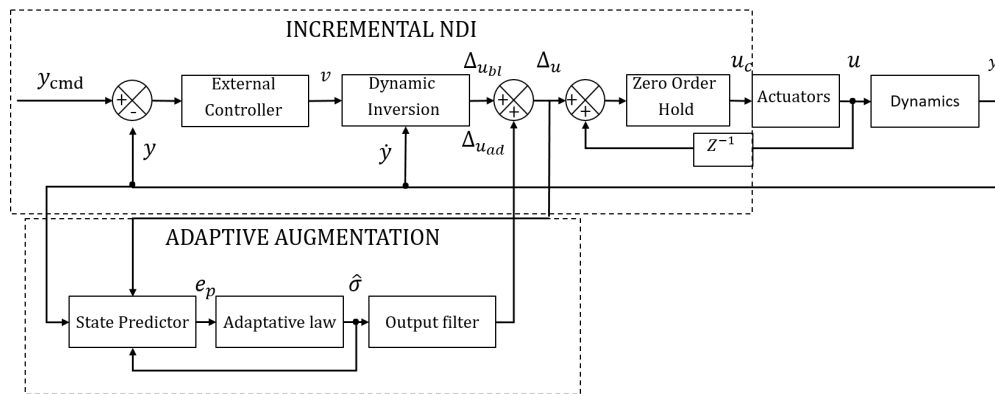

Fig. 13 $\mathcal{L}_1$ **adaptive augmentation architecture**

Where $\dot{x}_0 = z^{-1}\dot{x}$ is the last time step value of $\dot{x}$. In order to help the convergence of the predictor, a corrective proportional term to the prediction error is added to the predictor dynamics, where K_p is the proportional gain. The value of the matched uncertainties σ is replaced by its estimation from the adaptation law $\hat{\sigma}$. Additionally, the states of the systems are all considered observable and are measured.

$$\dot{\hat{x}} = z^{-1}\dot{x} + G_n \left(\Delta u + \hat{\sigma} \right) - K_p \left(\hat{x} - x \right) \tag{35}$$

$$\dot{\hat{y}} = z^{-1}\dot{y} + G_n \left(\Delta u + \hat{\sigma} \right) - K_p \left(\hat{y} - y \right) \tag{36}$$

The prediction error dynamics is defined by Eq. (37).

$$\begin{aligned} \dot{e}_p &= \dot{\hat{y}} - \dot{y} \\ &= -K_p e_p + G_n \left(\hat{\sigma} - \sigma \right) \end{aligned} \tag{37}$$

2. Adaptation Law

The piecewise constant adaptation law is first introduced in [28]. This adaption law is constant between two time steps and therefore the sampling frequency of the system influence directly the adaptation speed and accuracy. The authors in [8] have detailed the estimation of $\hat{\sigma}$ from the error dynamics. For the reader comprehension, the main steps of the adaptation law design are recalled. From Eq. (37), the prediction error at the next time step is defined as follows.

$$e_p(iT + t) = e^{-K_p t} e_p(iT) + \int_0^t e^{-K_p(t-\tau)} G_n \hat{\sigma}(iT) \mathrm{d}\tau \tag{38}$$

The objective is to find the expression of $\hat{\sigma}$ that will drive the prediction error to zero at the next time step.

$$\begin{aligned} & e_p(iT + t) = 0 \\ \Leftrightarrow\ & e^{-K_p T} e_p(iT) = -\int_0^t e^{-K_p(T-\tau)} G_n \hat{\sigma}(iT) \mathrm{d}\tau \\ \Leftrightarrow\ & e^{-K_p T} e_p(iT) = -\left[K_p^{-1} e^{-K_p(T-\tau)} G_n \hat{\sigma}(iT) \right]_0^T \\ \Leftrightarrow\ & e^{-K_p T} e_p(iT) = K_p^{-1} \left(e^{-K_p T} - \mathbb{I} \right) G_n \hat{\sigma}(iT) \end{aligned} \tag{39}$$

The variable $\Phi(iT)$ and $\mu(iT)$ are defined as follows and the final expression of the piecewise constant adaptation is obtained in Eq. (59).

$$\Phi(iT) = K_p^{-1} \left(e^{-K_p T} - \mathbb{I} \right) \tag{40a}$$

$$\mu(iT) = e^{-K_p T} e_p(iT) \tag{40b}$$

$$\hat{\sigma}(iT) = G_n^{-1} \Phi(iT)^{-1} \mu(iT) \tag{41}$$

3. Underlying Filter

This section recalled the main results from [10] and how the design of the low pass filter $C(s)$ influence the performance of the adaptive controller and its robustness. In Eq. (43a), y_{ref} is the non-adaptive version of this adaptive controller (without uncertainties) and r is the reference input. The parameter λ can be render arbitrary small by increasing the bandwidth of $C(s)$ and therefore reduce the gap between y_{ref} and y. $\lambda < 1$ guarantee the stability of the system with uncertainties under a predefined convex set Θ[24].

$$G(s) = (s\mathbb{I} - A_m)^{-1} b \left(1 - C(s) \right) \tag{42a}$$

$$\lambda = \|G(s)\|_{\mathcal{L}_1} \sigma_{\max} < 1 \tag{42b}$$

The performance of the adaptive controller can be enhanced by augmenting the bandwidth ω_c of the filter. However, a high bandwidth of $C(s)$, implies more high frequency in the control loop and reduce the delay margin. Asymptotically,

with τ the delay margin, the robustness similar to an MRAC is obtained.

$$\lim_{w_c \to \infty} \|y_{ref} - y\|_{\mathcal{L}_\infty} = \lim_{w_c \to \infty} \frac{\lambda}{1 - \lambda} \|c\|_{\mathcal{L}_1} \|G(s)\|_{\mathcal{L}_1} \|r\|_{\mathcal{L}_\infty} = 0 \tag{43a}$$

$$\lim_{w_c \to \infty} \tau = 0 \tag{43b}$$

The desired structure and the parameters of $C(s)$ can be obtained by trial and error or the optimal solution between performance (smallest λ) and maximum delay margin τ can be solved using LMI [29] or multi-objective optimization [30]. In the presented implementation, LMI constraints are used to obtain a minimal upper-bound for λ and thus guarantee satisfactory performance of the adaptation.

C. Roll Autopilot Augmentation

As explained is Section. III.A, without friction, the roll dynamic equations are already linear and therefore parametric uncertainties on the roll channel are not critical. More precisely, even in the presence of uncertainties, the INDI inner-loop transfer function will still be a chain of integrators, the only difference is that the chain of integrators does not have a unitary gain. In the end, a robust external controller with a sufficiently important gain margin can keep the system stable under a moderate range of uncertainties but may provide much lower performance. For this reasons, an adaptive augmentation is still relevant. The analytical expression of the INDI inversion for the roll channel in discrete time, with real actuators and under parametric uncertainties is given by Eq. (44).

$$\tilde{p}_2 = \left(\frac{\Delta G G_n^{-1} + 1}{\mathcal{Z}\{G_\delta(s)\}^{-1} + \Delta G G_n^{-1} \mathcal{Z}\{G_\delta(s)\}^{-1} + 1 - z^{-1}\mathcal{Z}\{G_\delta(s)\}} \right) v \tag{44a}$$

$$G_n = \begin{bmatrix} I_{x_2}^{-1}\overline{q}SdC_{l_\delta} \\ 0 \end{bmatrix} \tag{44b}$$

A focus is given on the design of the predictor and filter design because the design of the adaptation law depends only on the gains of the predictor K_p which are defined in the output predictor design subsection.

1. Output predictor design

The gains of the predictor K_p are tuned to obtained an identification time scale 5 to 10 times faster than the closed-loop dynamics to avoid interactions which could lead to instability. In equation (45) p are the poles of the roll channel closed-loop dynamics and p_e are the predictor poles.

$$\begin{aligned} p &= -13.3 \pm 10.7j \\ p_e &= -133 \pm 10.7j \end{aligned} \tag{45}$$

From the desired poles of the predictor and the state space representation of the roll dynamics (15), the gains of the predictor are obtained using classical linear estimator pole placement.

$$0 = \left| s\mathbb{I} - \left(A - K_P C\right) \right| \tag{46a}$$

$$K_p = \begin{bmatrix} 133 & -10.7 \\ 11.7 & 133 \end{bmatrix} \tag{46b}$$

$$\begin{bmatrix} \dot{\hat{p}}_2 \\ \dot{\hat{\phi}}_2 \end{bmatrix} = \begin{bmatrix} \dot{p}_2 \\ p_2 \end{bmatrix} + \begin{bmatrix} I_{x_2}^{-1}\overline{q}SdC_{l_\delta} \\ 0 \end{bmatrix} \left(\delta_p + \hat{\sigma}\right) - \begin{bmatrix} 133 & -10.7 \\ 11.7 & 133 \end{bmatrix} \begin{bmatrix} \hat{p}_2 - p_2 \\ \hat{\phi}_2 - \phi_2 \end{bmatrix} \tag{47}$$

2. LMI-based filter design

LMI optimization is used to obtain the parameters of the underlying filter A_f, b_f, c_f that will guarantee minimal upper bound for λ. In the following generalized eigenvalue problem λ is the decision variable to minimize.

$$\Phi(\alpha, P_1, P_2, M, q) \le 0 \tag{48a}$$

$$P_1 \le \lambda\mathbb{I} \tag{48b}$$

15

where

$$\Phi(\alpha, P_1, P_2, M, q) = \begin{bmatrix} \begin{bmatrix} A_m P_1 + P_1 A_m^\top + \alpha P_1 & -bq^\top \\ -qb^\top & M + M^\top + \alpha P_2 \end{bmatrix} & \begin{bmatrix} b \\ b_f \end{bmatrix} \\ \begin{bmatrix} b^\top & b_f^\top \end{bmatrix} & -\alpha \end{bmatrix} \tag{49}$$

In Eq. 48, $P_1 \in \mathbb{R}^{n \times n}$ and $P_2 \in \mathbb{R}^{n_f \times n_f}$ are positive definite matrices, $q \in \mathbb{R}^{n_f}$ is a vector, $M \in \mathbb{R}^{n_f \times n_f}$ is a matrix and $\alpha \in \mathbb{R}^+$ is bounded as $0 < \alpha < -2\Re(\lambda_{\max}(A_m))$ The parameters of the filter are obtained from the solution of Eq. 48.

$$A_f = M P_2^{-1} \quad c_f = P_2^{-1} q \quad b_f = [0 \quad -1]^\top \tag{50}$$

With $\alpha = 32.5$ and Am and b the state space representation of the roll channel closed-loop dynamics, the filter in Eq.(51) is obtained guaranteeing $\lambda < 1$. $C(s)$ is then discretized using Tustin's bilinear transform to obtain $C_d(z)$.

$$C(s) = \frac{-414s^2 - 13670s - 11280}{s^3 + 447.2s^2 + 13940s + 11280} \tag{51}$$

$$C_d(z) = \frac{-0.4082 + 0.3645z^{-1} + 0.407z^{-2} - 0.3657z^{-3}}{1 - 2.076z^{-1} + 1.243z^{-2} - 0.1641z^{-3}} \tag{52}$$

3. Simulation results

For the analysis of the performance of the proposed $\mathcal{L}_1$ adaptive augmentation, two simulation scenarios are presented. In Fig. 14, where σ is the real value of the uncertainties and $\hat{\sigma}$ is its estimation from the adaptation law, an acceptable and realistic level of uncertainties is introduced in the system. In this simulation both the baseline and the adaptive augmentation are close to the reference model. The uncertainties on the dynamic pressure $\bar{q}$ and the aerodynamic coefficient C_{l_δ} affects the control input of the system but it is still linear Eq. (44) that's why the baseline autopilot achieve acceptable performance. In Fig. 15, a much higher level of parametric uncertainties is introduced in the system which may not be realistic but it demonstrated the capacity of the adaptive augmentation to keep a high performance level where the performance of the baseline would have been very degraded. In this situation, the real control authority of the system is much less than the nominal case, then the baseline autopilot doesn't provide enough amplitude on the control signal, the compensation is made from the adaptive part which estimate from the prediction error the difference between the real and nominal control effectiveness.
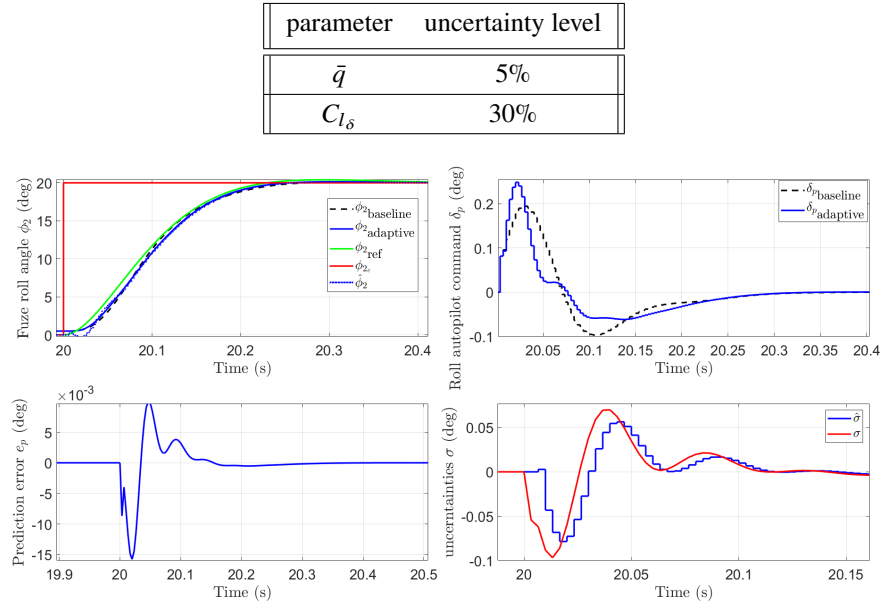
parameter	uncertainty level
$\bar{q}$	5%
C_{l_δ}	30%

Fig. 14   Performance comparison between the roll baseline autopilot and the $\mathcal{L}_1$ adaptive augmentation

16

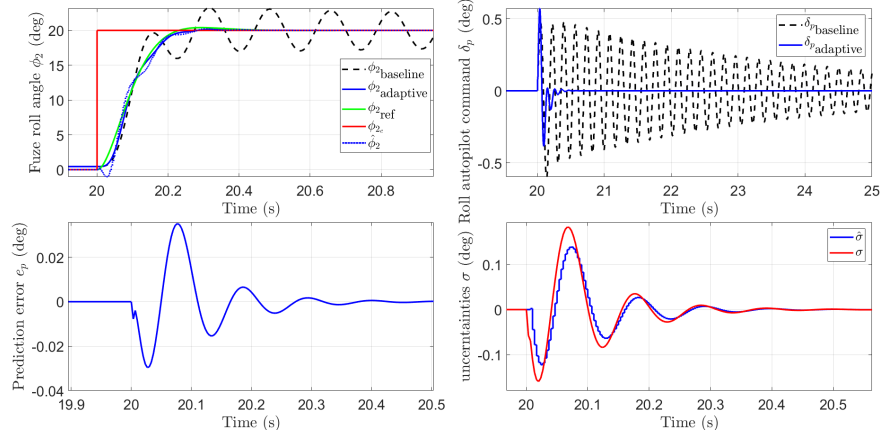| parameter	uncertainty level
$\bar{q}$	45%
C_{l_δ}	50%

Fig. 15   Performance comparison between the roll baseline autopilot and the $\mathcal{L}_1$ adaptive augmentation

D. Lateral rate autopilot Augmentation

Nonlinear simulations of the lateral channel autopilot in Fig. 10 show the impact of implementation constraints on the INDI inversion. As a matter of fact, Eq. (22) reveals the expression of the inversion error which depends on the flight parameters, the actuators dynamics and sampling frequency.

$$\begin{bmatrix} \tilde{q} \\ \tilde{r} \end{bmatrix} = \left(\frac{\mathcal{Z}\{G_\delta(s)\} - z}{z\mathcal{Z}\{G_\delta(s)\}} \right) \begin{bmatrix} \frac{\bar{q}SdC_{m_\delta}}{\bar{I}_t} & 0 \\ 0 & \frac{\bar{q}SdC_{m_\delta}}{\bar{I}_t} \end{bmatrix} \begin{bmatrix} \delta_q \\ \delta_r \end{bmatrix} + \begin{bmatrix} v_q \\ v_r \end{bmatrix}$$

$$\Leftrightarrow \begin{bmatrix} \tilde{q} \\ \tilde{r} \end{bmatrix} = \begin{bmatrix} \epsilon_q \\ \epsilon_r \end{bmatrix} + \begin{bmatrix} v_q \\ v_r \end{bmatrix} \tag{53}$$

Two approaches are investigated in order to cancel the inversion error of the lateral channel. The first approach consists of cancelling $\begin{bmatrix} \epsilon_q & \epsilon_r \end{bmatrix}^\top$ online by modifying the pseudo-control variables $\begin{bmatrix} v_q & v_r \end{bmatrix}^\top$ given by Eq. 52. The figure 16 shows the INDI controller architecture with the inversion correction, Fig. 17 and Fig. 18 show the effect of the inversion correction on the closed-loop dynamics of the lateral channels. It can be seen that this approach provide successful results by attenuating drastically the coupling between the channels. However this approach has two main drawbacks that renders it difficult to implement in a real conditions. First, this technique is not robust to parameter uncertainties, indeed parameters used in Eq. (53) can be subjected to a large range of uncertainties and therefore the estimated inversion error can diverge from the real one to be cancelled. Second, this approach needs time-scale separation between the control loop and the inversion correction. Consequently, this technique has only shown successful results with slow external controller (more than 1.5 second settling time) which is five times slower than the desired settling time. For all this reasons, another approach is preferred based on the same $\mathcal{L}_1$-adaptive augmentation as for the roll channel with a slight modification of the output predictor in order to take into account the inversion error.

$$\begin{bmatrix} v_q \\ v_r \end{bmatrix} = \begin{bmatrix} \tilde{q}_{\text{des}} \\ \tilde{r}_{\text{des}} \end{bmatrix} - \begin{bmatrix} \epsilon_q \\ \epsilon_r \end{bmatrix} \tag{54}$$

1. Output predictor modification

The output predictor of the $\mathcal{L}_1$-adaptive augmentation for the lateral channels is slightly modified in order to better counteract the effects of the inversion error. The goal is to use the desired dynamics $\begin{bmatrix} v_q & v_r \end{bmatrix}^\top$ instead of the estimated
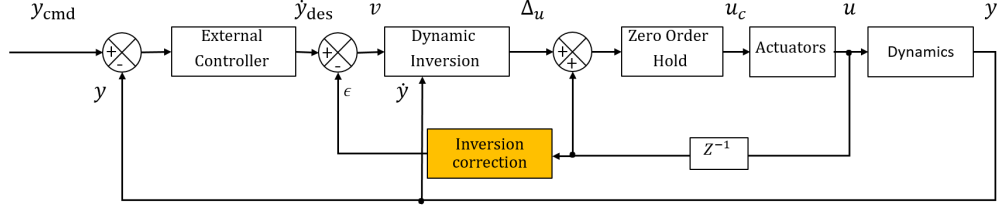
Fig. 16   INDI architecture with inversion error correction
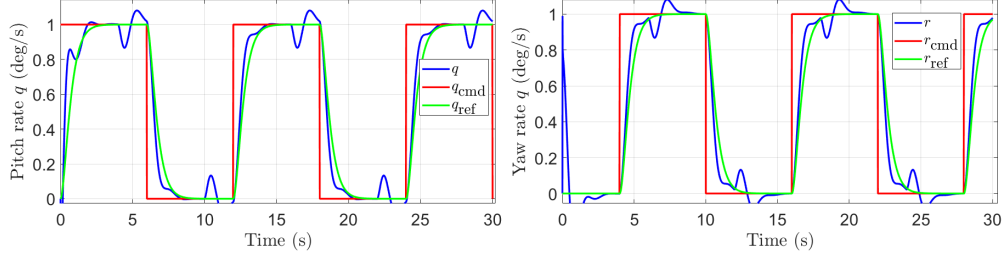

Fig. 17   Lateral channels closed-loop behaviour without inversion correction
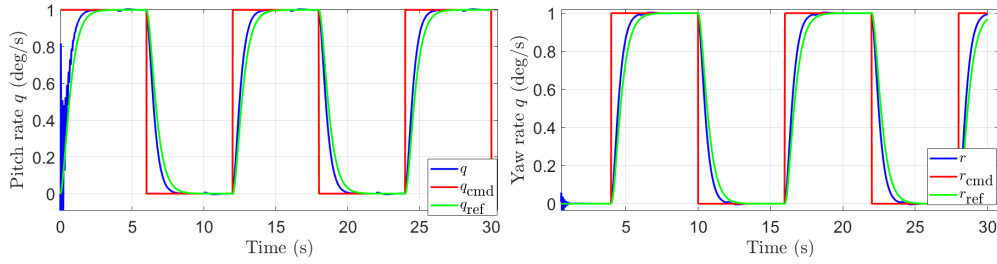

Fig. 18   Lateral channels closed-loop behaviour with inversion correction

output derivative $[\tilde{q} \quad \tilde{r}]^\top$. In this manner, the predictor given by Eq.(53) is based on the desired dynamics and therefore the inversion error is estimated from the adaptation law. In the same way as for the roll channel, proportional gains $K_{PY} = 48$ are used to help the convergence of the prediction error

$$\dot{\hat{y}} = v + G_n\left(\Delta u + \hat{\sigma}\right) - K_{PY}\left(\hat{y} - y\right)$$

$$\Leftrightarrow \begin{bmatrix} \dot{\hat{q}} \\ \dot{\hat{r}} \end{bmatrix} = \begin{bmatrix} v_q \\ v_r \end{bmatrix} + \begin{bmatrix} \dfrac{\overline{q}SdC_{m_\delta}}{\tilde{I}_t} & 0 \\ 0 & \dfrac{\overline{q}SdC_{m_\delta}}{\tilde{I}_t} \end{bmatrix}\left(\begin{bmatrix} \delta_q \\ \delta_r \end{bmatrix} + \begin{bmatrix} \hat{\sigma}_q \\ \hat{\sigma}_r \end{bmatrix}\right) - \begin{bmatrix} 48 & 0 \\ 0 & 48 \end{bmatrix}\begin{bmatrix} \hat{q} - q \\ \hat{r} - r \end{bmatrix}. \tag{55}$$

2. Filter design

The same LMI optimization as for the roll channel is used to obtain the output filter $C(s)$ for the lateral channel using $\alpha = 29$. The adaptive incremental control signal $\Delta_{u_{ad}}$ obtained in Eq.56 where $C_d(z)$ is the Z-transform of C(s) using Tustin's bilinear transformation are given below

$$\Delta_{u_{ad}} = Cd(z)\sigma \tag{56}$$

$$C_d(z) = \frac{-0.3619 - 0.3619z^{-1}}{1 - 0.2762z^{-1}}. \tag{57}$$
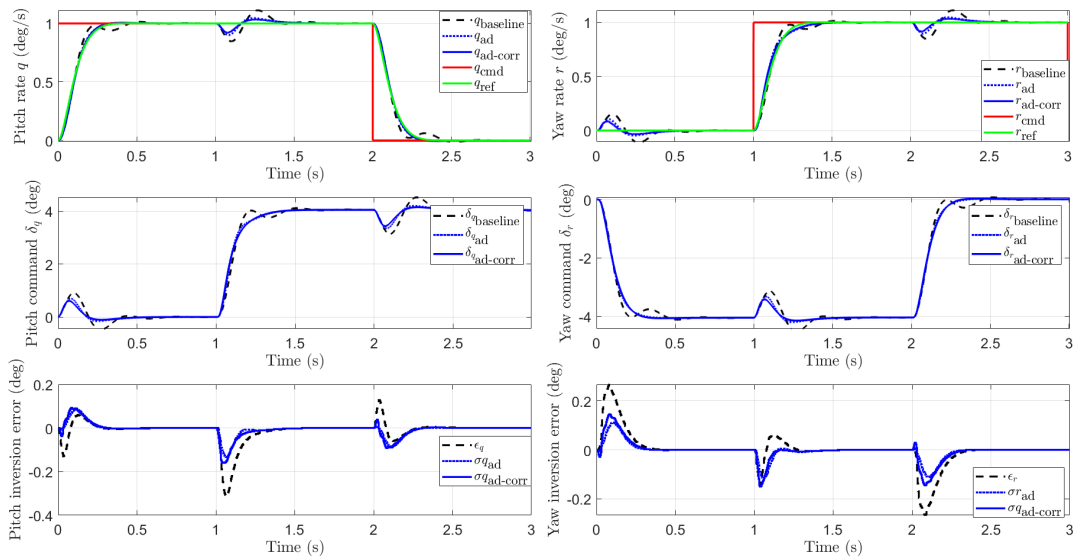
18

Fig. 19   Performance comparison between the baseline and the adaptive lateral rate autopilot in nominal conditions

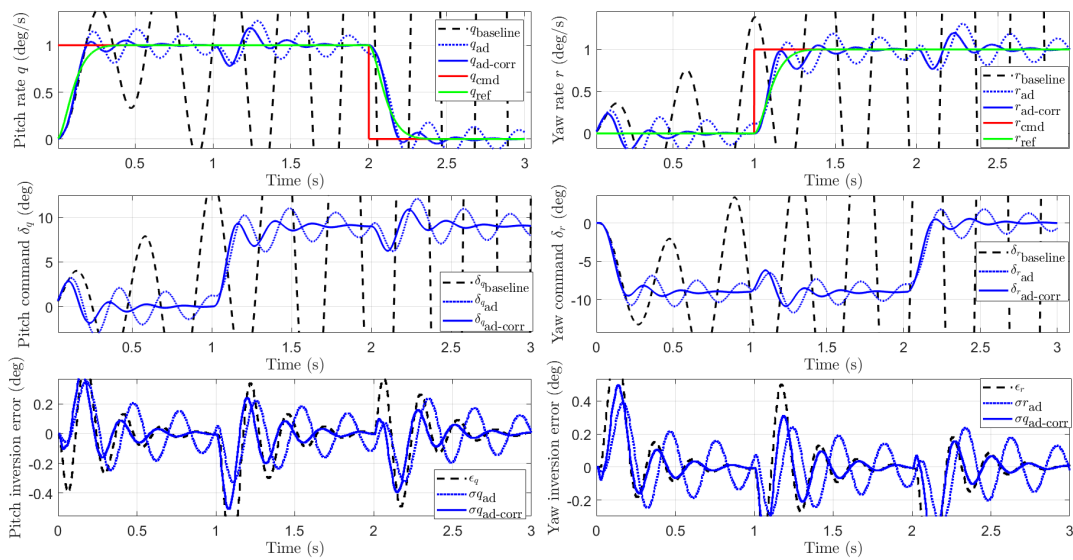| parameter	uncertainty level
$\bar{q}$	20%
C_{m_δ}	45%

Fig. 20   Performance comparison between the baseline and the adaptive lateral rate autopilot in degraded scenario

3. Simulation results

For the performance analysis of the $\mathcal{L}_1$-adaptive augmentation of the lateral channel autopilot, two scenarios are proposed. Fig. 19 compares the performance between a baseline autopilot with an external controller tuned considering perfect inversion and its adaptive augmentation. It can be noticed that even without introducing uncertainties, the adaptive augmentation improves the performance of the autopilot by cancelling a part of the inversion error. The performance are slightly better with the modified state predictor. In another part, Fig. 20 proposes a degraded scenario and shows the capacity of the adaptive augmentation to keep the stability of the system and with improved performance using the modified state predictor.

E. Load factor autopilot Augmentation

The design of the $\mathcal{L}_1$-augmentation for the load factor autopilot is very similar to the lateral rate autopilot augmentation detailed is Section IV.D without the need to modify the sate predictor because the coupling between the lateral load factors is negligible. To avoid any redundancy and for the conciseness of the paper, the design of the Load factor autopilot augmentation will not be detailed. The equation (56) and (57) describe the output predictor and the filter obtained using LMI respectively. Similarly to Section IV.D.3, the performance of the adaptive augmentation of the load factor autopilot is assessed by introducing a significant amount of parametric uncertainties in the model.

$$\begin{bmatrix} \hat{\dot{n}}_z \\ \hat{\dot{n}}_y \end{bmatrix} = \begin{bmatrix} \dot{n}_z \\ \dot{n}_y \end{bmatrix} + \frac{\bar{q}S}{gm} \begin{bmatrix} -C_{N_\delta} - C_{N_\alpha} & (\tan\theta - \alpha)\beta\left(C_{N_\delta} - C_{N_\alpha}\right) - (\tan\theta\alpha + 1)\left(\frac{p_1 d}{2V}C_{Yp_\alpha}\right) \\ \left(\frac{p_1 d}{2V}\right)C_{Yp_\alpha} & (\tan\theta\alpha + 1)\left(C_{N_\delta} + C_{N_\alpha}\right) + (\tan\theta - \alpha)\left(\frac{p_1 d}{2V}\right)C_{Yp_\alpha}\beta \end{bmatrix} \begin{bmatrix} q + \hat{\sigma}_{nz} \\ r + \hat{\sigma}_{ny} \end{bmatrix} - \begin{bmatrix} 7.5 & 0 \\ 0 & 7.5 \end{bmatrix} \begin{bmatrix} \hat{n}_z - n_z \\ \hat{n}_y - n_y \end{bmatrix}$$

(58)

$$C_d(z) = \frac{-0.06855 - 0.06855z^{-1}}{1 - 0.8629z^{-1}}$$

(59)

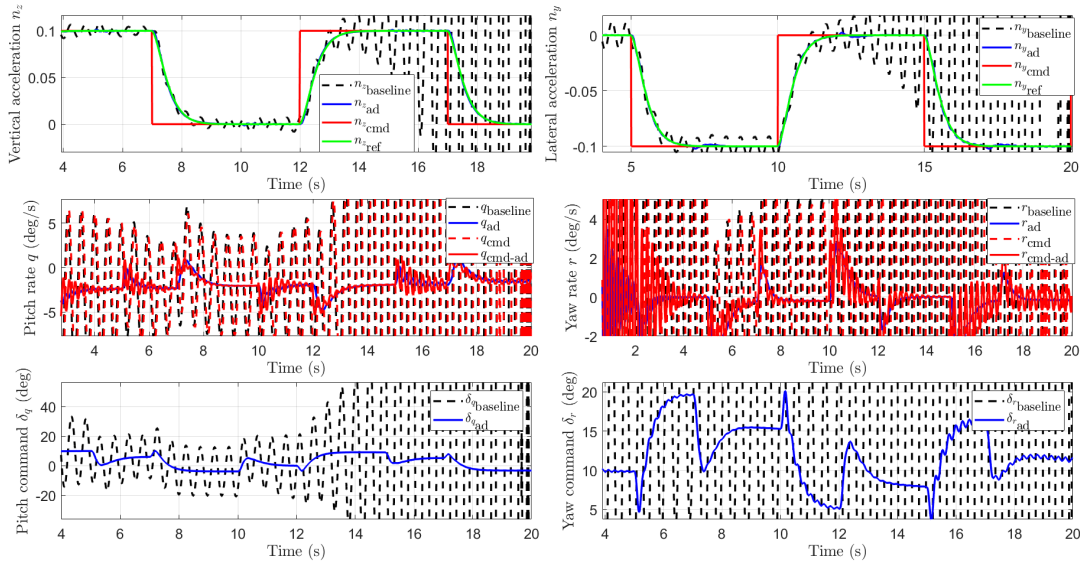| parameter	uncertainty level
C_A	30%
C_{N_α}	80%
C_{Yp_α}	70%
C_{N_δ}	70%
C_{m_δ}	80%

Fig. 21   Performance comparison between the baseline and the adaptive load factor autopilot in degraded scenario

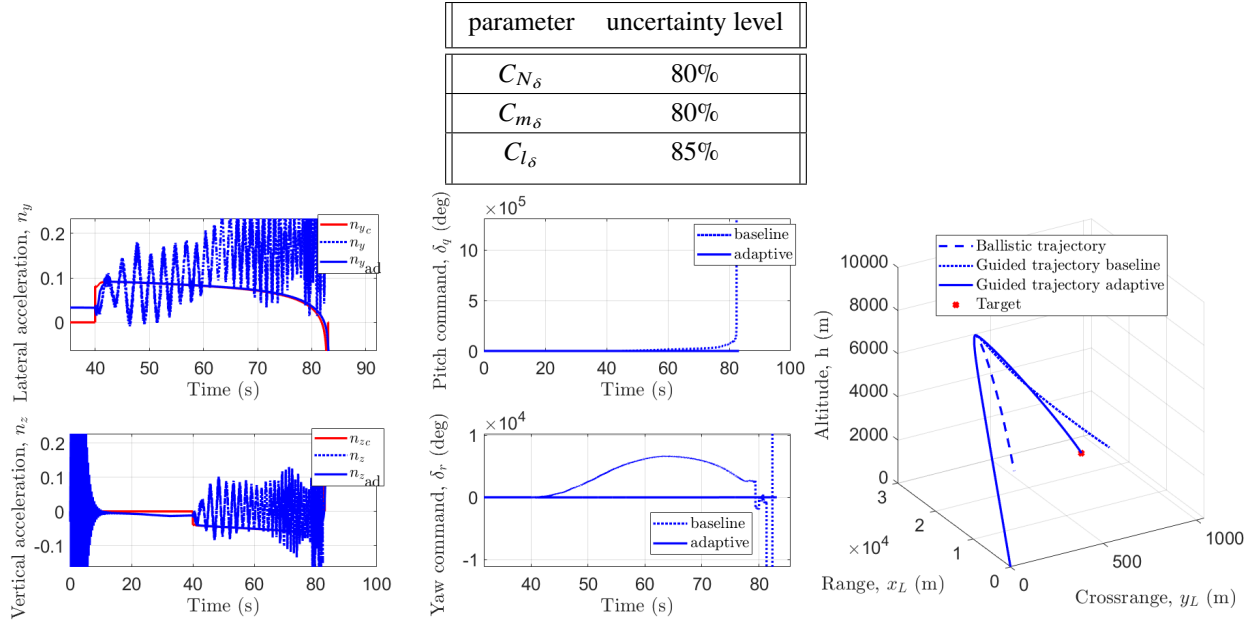| parameter	uncertainty level
C_{N_δ}	80%
C_{m_δ}	80%
C_{l_δ}	85%

Fig. 22   Performance comparison between the baseline and the adaptive autopilot on a full trajectory

F. Full trajectory simulation

The figure 22 compares the performance between the baseline load factor autopilot and its adaptive augmentation during a guided trajectory scenario. The objective is to compare only the performance of the two controllers, however uncertainties on some aerodynamic coefficient (drag, lift, Magnus) affect also the implemented guidance law. To this end, in this simulation, uncertainties are only considered on the canards aerodynamics coefficients (C_{N_δ},C_{m_δ},C_{l_δ}). Consequently, the guidance law is still functioning in nominal conditions whereas this autopilot is subjected to significant uncertainties. This guided phase is launched after the apogee at $t = 40$s. It can be noticed that the baseline control signal is divergent and the projectile's load factors are oscillating, it result that the projectile crash at several hundred meters of the target which is less than the unguided shot but significantly less accurate than in nominal conditions (Fig. 12). In the other hand, the $\mathcal{L}_1$-adaptive augmented autopilot achieve to follow the desired load factors and reduce successfully the ballistic dispersion.

V. Conclusion

In this article, the design of an $\mathcal{L}_1$-adaptive augmented INDI autopilot applied to a class of dual-spin projectiles is presented. Nonlinear simulation results show the capacity of the baseline to reduce the ballistic dispersion of the projectile in nominal scenario, however parameter uncertainties significantly impact the tracking performance of the control law. On the other hand, analytical results demonstrate the impact of actuator speed and sampling frequency on INDI inversion. To counteract this two phenomena, an $\mathcal{L}_1$-adaptive augmentation scheme has been implemented and reveals to improve the tracking performance of the autopilot over a large range of parameter uncertainties. Further investigations and robustness analysis must be conducted on the adaptive augmentation in order to guarantee tracking performance bounds.

References

[1] Jitpraphai, T., and Costello, M., "Dispersion Reduction of a Direct Fire Rocket Using Lateral Pulse Jets," *Journal of Spacecraft and Rockets*, Vol. 38, No. 6, 2001, pp. 929–936. https://doi.org/10.2514/2.3765.

[2] Sève, F., Theodoulis, S., Wernert, P., Zasadzinski, M., and Boutayeb, M., "Gain-Scheduled $\mathcal{H}_\infty$ Loop-Shaping Autopilot Design for Spin-Stabilized Canard-Guided Projectiles," *AerospaceLab Journal*, Vol. 13, 2017. https://doi.org/10.12762/2017.AL13-03.

[3] Thai, S., Theodoulis, S., Roos, C., Biannic, J.-M., and Proff, M., "Gain-Scheduled Autopilot Design with Anti-Windup Compensator for a Dual-Spin Canard-Guided Projectile," *2020 IEEE Conference on Control Technology and Applications (CCTA)*, IEEE, 2020.

[4] Leith, D. J., and Leithead, W. E., "Survey of gain-scheduling analysis and design," *International Journal of Control*, Vol. 73, No. 11, 2000. https://doi.org/10.1080/002071700411304.

[5] Smeur, E. J. J., Chu, Q., and de Croon, G. C. H. E., "Adaptive Incremental Nonlinear Dynamic Inversion for Attitude Control of Micro Air Vehicles," *Journal of Guidance, Control, and Dynamics*, Vol. 39, No. 3, 2016, pp. 450–461. https://doi.org/10.2514/1.g001490.

[6] Grondman, F., Looye, G., Kuchar, R. O., Chu, Q. P., and Kampen, E.-J. V., "Design and Flight Testing of Incremental Nonlinear Dynamic Inversion-based Control Laws for a Passenger Aircraft," *2018 AIAA Guidance, Navigation, and Control Conference*, American Institute of Aeronautics and Astronautics, 2018. https://doi.org/10.2514/6.2018-0385.

[7] Sieberling, S., Chu, Q. P., and Mulder, J. A., "Robust Flight Control Using Incremental Nonlinear Dynamic Inversion and Angular Acceleration Prediction," *Journal of Guidance, Control, and Dynamics*, Vol. 33, No. 6, 2010. https://doi.org/10.2514/1.49978.

[8] Bhardwaj, P., Akkinapalli, V. S., Zhang, J., Saboo, S., and Holzapfel, F., "Adaptive Augmentation of Incremental Nonlinear Dynamic Inversion Controller for an Extended F-16 Model," *AIAA Scitech 2019 Forum*, American Institute of Aeronautics and Astronautics, 2019. https://doi.org/10.2514/6.2019-1923, URL https://doi.org/10.2514/6.2019-1923.

[9] Harris, J., and Valasek, J., "Direct $\mathcal{L}_1$-Adaptive Nonlinear Dynamic Inversion Control for Command Augmentation Systems, booktitle = 2018 AIAA Guidance, Navigation, and Control Conference," American Institute of Aeronautics and Astronautics, 2018. https://doi.org/10.2514/6.2018-1575.

[10] Cao, C., and Hovakimyan, N., "Stability Margins of $\mathcal{L}_1$ Adaptive Controller: Part II," *2007 American Control Conference*, IEEE, 2007. https://doi.org/10.1109/acc.2007.4282486, URL https://doi.org/10.1109/acc.2007.4282486.

[11] Costello, M., and Peterson, A., "Linear Theory of a Dual-Spin Projectile in Atmospheric Flight," *Journal of Guidance, Control, and Dynamics*, Vol. 23, No. 5, 2000. https://doi.org/10.2514/2.4639.

[12] Zipfel, P. H., *Modeling and Simulation of Aerospace Vehicle Dynamics, Third Edition*, American Institute of Aeronautics and Astronautics, Inc., 2014. https://doi.org/10.2514/4.102509.

[13] Pineau, S., Theodoulis, S., Zasadzinski, M., and Boutayeb, M., "Terminal Phase Nonlinear Attitude Autopilot Design For Dual-Spin Guided Projectiles," *CEAS EuroGNC*, 2022.

[14] Pineau, S., Theodoulis, S., Zasadzinski, M., and Boutayeb, M., "Autopilot Design for Dual-Spin Projectiles using Incremental Nonlinear Dynamic Inversion," *IEEE Mediterranean Conference on Control and Automation*, 2022.

[15] Stevens, B. L., Lewis, F. L., and Johnson, E. N., *Aircraft Control and Simulation: Dynamics, Controls Design, and Autonomous Systems*, John Wiley & Sons, Inc, 2015. https://doi.org/10.1002/9781119174882.

[16] Skogestad, S., and Postlethwaite, I., *Multivariable Feedback Control: Analysis and Design*, paperback ed., Wiley-Interscience, 2005.

[17] Proff, M., and Theodoulis, S., "Study of Impact Point Prediction Methods for Zero-Effort-Miss Guidance: Application to a 155mm Spin-Stabilized Guided Projectile," *CEAS EuroGNC*, 2019.

[18] Menon, P., Iragavarapu, V., Ohlmeyer, E., Menon, P., Iragavarapu, V., and Ohlmeyer, E., "Nonlinear missile autopilot design using time-scale separation," *Guidance, Navigation, and Control Conference*, American Institute of Aeronautics and Astronautics, 1997. https://doi.org/10.2514/6.1997-3765.

[19] Jafarnejadsani, H., Sun, D., Lee, H., and Hovakimyan, N., "Optimized L1 Adaptive Controller for Trajectory Tracking of an Indoor Quadrotor," *Journal of Guidance, Control, and Dynamics*, Vol. 40, No. 6, 2017, pp. 1415–1427. https://doi.org/10.2514/1.g000566.

[20] Peter, F., Holzapfel, F., Xargay, E., and Hovakimyan, N., "L1 Adaptive Augmentation of a Missile Autopilot," *AIAA Guidance, Navigation, and Control Conference*, American Institute of Aeronautics and Astronautics, 2012. https://doi.org/10.2514/6.2012-4832.

[21] Whitaker, H., Yamron, J., Kezer, A., and Laboratory, M. I. o. T. I., *Design of Model-reference Adaptive Control Systems for Aircraft*, Report Massachusetts Institute of Technology Instrumentation Laboratory R, M.I.T. Instrumentation Laboratory, 1958.

[22] Osburn, P., *New Developments in the Design of Model Reference Adaptive Control Systems*, IAS papers, Institute of the Aerospace Sciences, 1961.

[23] Ioannou, P., and Kokotovic, P., "Robust redesign of adaptive control," *IEEE Transactions on Automatic Control*, Vol. 29, No. 3, 1984, pp. 202–211. https://doi.org/10.1109/tac.1984.1103490.

[24] Hovakimyan, N., and Cao, C., $\mathcal{L}_1$ *Adaptive Control Theory: Guaranteed Robustness with Fast Adaptation*, SIAM, Philadelphia, 2010.

[25] Gregory, I., Cao, C., Xargay, E., Hovakimyan, N., and Zou, X., "L1 Adaptive Control Design for NASA AirSTAR Flight Test Vehicle," *AIAA Guidance, Navigation, and Control Conference*, American Institute of Aeronautics and Astronautics, 2009. https://doi.org/10.2514/6.2009-5738.

[26] Ackerman, K., Xargay, E., Choe, R., Hovakimyan, N., Cotting, M. C., Jeffrey, R. B., Blackstun, M. P., Fulkerson, T. P., Lau, T. R., and Stephens, S. S., "L1 Stability Augmentation System for Calspan's Variable-Stability Learjet," *AIAA Guidance, Navigation, and Control Conference*, American Institute of Aeronautics and Astronautics, 2016. https://doi.org/10.2514/6.2016-0631.

[27] Choe, R., Stroosma, O., Xargay, E., Damveld, H., Hovakimyan, N., Mulder, J., and Damveld, H., "A Handling Qualities Assessment of a Business Jet Augmented with an L1 Adaptive Controller," *AIAA Guidance, Navigation, and Control Conference*, American Institute of Aeronautics and Astronautics, 2011. https://doi.org/10.2514/6.2011-6610.

[28] Cao, C., and Hovakimyan, N., "L1 Adaptive Output-Feedback Controller for Non-Strictly-Positive-Real Reference Systems: Missile Longitudinal Autopilot Design," *Journal of Guidance, Control, and Dynamics*, Vol. 32, No. 3, 2009, pp. 717–726. https://doi.org/10.2514/1.40877.

[29] Li, D., Hovakimyan, N., Cao, C., and Wise, K., "Filter Design for Feedback-loop Trade-off of L_1 Adaptive Controller: A Linear Matrix Inequality Approach," *AIAA Guidance, Navigation and Control Conference and Exhibit*, American Institute of Aeronautics and Astronautics, 2008. https://doi.org/10.2514/6.2008-6280.

[30] Li, D., Patel, V., Cao, C., Hovakimyan, N., and Wise, K., "Optimization of the Time-Delay Margin of L1 Adaptive Controller via the Design of the Underlying Filter," *AIAA Guidance, Navigation and Control Conference and Exhibit*, American Institute of Aeronautics and Astronautics, 2007. https://doi.org/10.2514/6.2007-6646.